STRAIN SENSITIVITY ENHANCEMENT FOR THE HOLE-DRILLING RESIDUAL STRESSES MEASUREMENT METHOD

by

MOHAMMAD TOOTOONIAN
B.Sc., Tehran University, Iran, 1980

A THESIS SUBMITTED IN PARTIAL FULFILLMENT OF
THE REQUIREMENTS FOR THE DEGREE OF
MASTER OF APPLIED SCIENCE
in
THE FACULTY OF GRADUATE STUDIES
(Department of Mechanical Engineering)

We accept this thesis as conforming
to the required standard

THE UNIVERSITY OF BRITISH COLUMBIA

December 1993

In presenting this thesis in partial fulfilment of the requirements for an advanced degree at the University of British Columbia, I agree that the Library shall make it freely available for reference and study. I further agree that permission for extensive copying of this thesis for scholarly purposes may be granted by the head of my department or by his or her representatives. It is understood that copying or publication of this thesis for financial gain shall not be allowed without my written permission.

Department of Mechanical Engineering

The University of British Columbia
Vancouver, Canada

Date November, 3rd, 1993

ABSTRACT

Two methods for enhancing the strain sensitivity of the hole-drilling method for measuring residual stress fields were examined in this thesis. Such enhanced strain sensitivity is important because it improves the accuracy of the residual stress evaluation. The first method involves enlarging the effective hole size by drilling a reverse taper hole. A simple practical technique for drilling reverse taper holes is described. The strain sensitivity for this new method is compared with that of the conventional hole-drilling method. Experimental results show excellent correspondence with theoretical results. The reasons for the sensitivity improvement are explained. The second method involves designing a 6-element strain gauge rosette. It is shown that the new 6-element rosette significantly enhances the strain sensitivity of the hole-drilling method. Experimental results show excellent agreement with predicted results. Moreover, it is shown that this new rosette improves the accuracy of the method concerning the measurement of the variation of residual stresses with depth.

TABLE OF CONTENTS

LIST OF FIGURES

NOMENCLATURE

$\bar{a}$, $\bar{b}$ = normalized form of the calibration coefficients $\overline{A}$, $\overline{B}$

a_i, b_i = calibration coefficients $\bar{a}$ and $\bar{b}$ corresponding to a hole i increments deep

$\bar{a}_{ij}$, $\bar{b}_{ij}$ = calibration coefficients for j increment within a hole i increments deep

$[\bar{a}]$, $[\bar{b}]$ = matrix form of the calibration coefficients $\bar{a}$ and $\bar{b}$ which have $\bar{a}_{ij}$ and $\bar{b}_{ij}$ as their elements

A, B = calibration coefficients for infinitesimal relieved strains

$\overline{A}$, $\overline{B}$ = calibration coefficients

C_{Ai}, C_{Bi} = condition numbers of matrices $[\bar{a}]$ and $[\bar{b}]$

F_{Ai}, F_{Bi} = stress evaluation reliability factors

E = Young's modulus of elasticity

h = hole depth

r_a = hole radius for straight holes and surface hole radius for tapered holes

r_i = inner radius of a strain gauge rosette

r_m = mean radius of a strain gauge rosette

ε = relieved strain measured by the strain gauge

ε_1 = strains measured by the strain gauge 1

ε_2 = strains measured by the strain gauge 2

ε_3 = strains measured by the strain gauge 3

ε_h = average (over the strain gauge grid) strain due to hydrostatic stress

ε_s = average (over the strain gauge grid) strain due to shear stress

ε_i = total measured relieved strain for i increments deep hole

ν = Poisson's ratio

φ = angular coordinate of the radial mid axis of the strain gauge measured counterclockwise from the maximum principal stress

φ_j = angular coordinate of the radial mid axis of the strain gauge measured counterclockwise from the maximum principal stresses at j increment

σ_{max} = maximum principal residual stress

σ_{min} = minimum principal residual stress

$\sigma_{max\,j}$ = maximum principal residual stress at the increment j

$\sigma_{min\,j}$ = minimum principal residual stress at the increment j

ACKNOWLEDGMENT

This thesis is dedicated to my wife, Mahnaz. Your love, patience and encouragement have made it possible.

I would like to thank my supervisor Dr. Gary Schajer for his invaluable guidance and enormous patience. I am thankful to Mr. Len Drakes, Mr. Tony Besic, and Mr. Anton Schreinders who professionally manufactured the necessary equipment and samples.

This study was financially supported by the Natural Science and Engineering Research Council of Canada (NSERC).

CHAPTER 1

INTRODUCTION

1.1 Residual Stresses

Residual stresses are stresses that exist in a material in the absence of any external loads. They can be induced in almost every step of most manufacturing processes. Usually, a permanent dimensional change in a portion of a work-piece is the source of the residual stresses. This dimensional change can occur by a plastic deformation, for example, during rolling, forming, and machining. Plastic deformation also can be caused by the large temperature gradients that occur during welding, heat treating or sintering. Elastic deformation also can be a source of dimensional changes and residual stresses, for example by tight fitting of assembled components or by solid-state phase transformations.

Residual stresses can significantly affect the serviceability of engineering components. The influence of residual stresses on fatigue strength is well known. Fracture, surface corrosion, and crack propagation are also directly influenced by to distribution of residual stresses in materials. Residual stresses are one of the important causes of failure of materials. Residual stresses can be beneficial as well as detrimental. Compressive residual stresses are mostly considered beneficial and tensile stresses are generally detrimental. Dimensional stability of a piece is impaired by residual stresses, compressive or tensile.

Despite their significance, residual stresses are often ignored in design and manufacturing, mostly because they are difficult to evaluate. Ever-growing needs for enhanced reliable design of lighter and smaller but safer components demand a better understanding of residual stresses. Reliable methods for measurement of residual stresses are essential for studying these stresses.

Conventional methods for measuring stresses due to applied loads in experimental stress analysis may not be suitable for measuring residual stresses. In conventional methods relative stresses are measured, i.e., the applied stresses are measured by comparing the current state of stress or strain with the zero state of stress or strain (by removing or applying external loads). However, there are no external loads in the case of residual stresses. Thus, specialized stress measurement methods must be used. These methods are divided into two categories: non-destructive methods which measure the absolute state of stress, and destructive methods which involve removing some stressed materials [1].

1.2 Methods of Measurement of Residual Stresses

The non-destructive measurement methods generally measure the properties of material that are altered by the absolute state of the stress of the specimen. Often the relation between these properties and stresses are not fully established and the results of the measurements by non-destructive methods are subject to interpretation. The most commonly used of these methods is the X-ray method. Others include the ultrasonic, magneto-acoustic, photoelastic, and the neutron diffraction methods. Following are brief descriptions of the most widely used of these methods [1].

The X-ray method is by far the most developed and the most widely used of the non-destructive methods for measuring residual stresses. It uses X-ray diffraction to measure the distance between two crystallographic lattice layers. This distance is changed by the state of stress of the material. Despite its widespread use, the X-ray diffraction method has some limitations. For example, the small penetration range of X-rays only permits measuring the surface residual stresses. The neutron diffraction method that is similar to

the X-ray method, has its penetration range of several orders of magnitude larger than the X-ray method, but has a low precision due to weak sources of neutrons.

The ultrasonic method uses changes in the velocities of ultrasonic waves due to stresses as a basis to measure residual stresses. One of the shortcomings of this method is that the average stress is measured, and therefore sharp stress gradients cannot be measured.

A few well-known destructive methods for residual stress measurement are the dissection method, the ring core method, and the hole drilling method. These methods evaluate residual stresses by measuring strains or displacements caused by removal of stressed material.

The most powerful, and most destructive, method is the dissection method. In this method, the stressed material is dissected layer by layer and at each step the deformation of the remaining material due to the removal of the material is measured. The original residual stresses can then be calculated. The method is very time consuming and the sample is completely destroyed.

Unlike the dissection method, which involves complete destruction of the measurement area, the ring core and hole drilling methods cause much less damage. For that reason they are often referred to as "semi-destructive " methods. The ring core method involves cutting a small ring core in the stressed material and measuring the relieved strains on the surface of the material remaining in the ring. The original existing residual stresses then can be calculated from the measured relieved strain data. The hole drilling method is similar to core ring method in principle, however, instead of a ring core a small hole is drilled and the relieved strains around the hole are measured. The ring core method has a higher sensitivity than the hole drilling method. However the size of the annular ring is relatively large, causing more damage than the hole drilling method.

Moreover, the results are much less localized. In contrast the hole drilling method does relatively little damage to the specimen and it is capable of more localized residual stress measurement. In addition drilling a hole is easier than cutting a ring core.

Despite its relatively low sensitivity, the hole drilling method is the most widely used technique for measuring residual stresses. The popularity of the method is mostly due to its simplicity, reliability and ease of use.

1.3 The hole drilling method

The hole drilling method involves drilling a cylindrical hole at the point of interest in a stressed material, measuring the relieved strain (or displacement) around the hole and calculating the original stresses from these measured strains [2]. The hole drilling method was first introduced by Mathar in 1934 [3]. He used a mechanical extensometer to measure the displacements around a through hole in a stressed plate. For his calculation he used the well-known Kirsch [4] solution for the stress distribution around a small hole in a thin plate subject to uniform stress. The accuracy of the method used by Mathar was low because of the use of a mechanical extensometer. Soete and Vancrombrugge, in 1950, greatly improved the accuracy of the method by using electrical strain gauges, in place of the extensometer [5].

In 1956, Kelsey [6] published his investigation into using the hole drilling method to measure stress variation with depth. He was also the first to use blind holes instead of through holes. Previously, the use of through holes limited the method only to thin plates. The method gained became standardized in 1966, when Rendler and Vigness developed the method into a systematic and reproducible procedure [7]. Their work is used as a base

for the ASTM E837 [8] standard for hole drilling method. Figure 1 schematically shows a typical hole-drilling rosette.

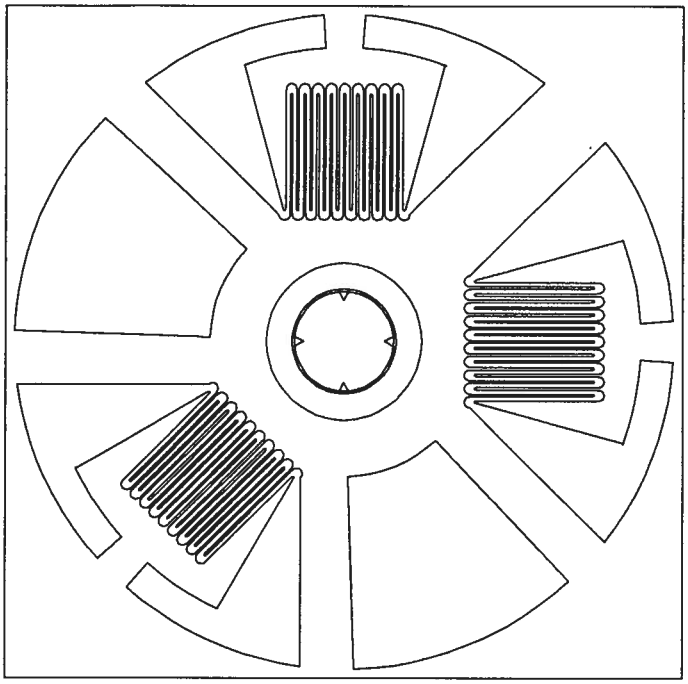

Figure 1 Typical strain gauge rosette for the hole-drilling method.

In 1974, Beaney and Procter [9] improved the practical aspect of the method by using air abrasive machining to enable stress free hole drilling. Flaman [10] developed the use of ultra high speed drilling to achieve stress free hole.

Schajer [11], in 1981, provided the first comprehensive finite element analysis of the method. Later in 1988, he published his systematic investigation on using the hole drilling method for determination of residual stress variation with depth and provided the finite element analysis for the case [12].

The technical literature on the hole drilling method is extensive and continues to grow.

1.4 Objective and overview of the study

Despite its widespread use and popularity, however, a weakness of the hole drilling method is that the measured strain reliefs are quite modest in size. The inevitable small experimental errors that occur may not be trivial compared with the measured strains. In such cases, the small errors could significantly impair the accuracy of the computed residual stresses.

In most hole-drilling measurements, it is assumed that the stresses in the specimen material do not vary with depth from the measured surface. However, in recent years, considerable interest has arisen for using the hole-drilling method to determine residual stresses that vary with depth from the measured surface. The associated stress calculations are numerically very sensitive, and even quite small strain measurement errors can have devastating effects on the accuracy of the results. Thus, in the non-uniform stress case, it is especially important to make the strain sensitivity of the hole-drilling method as high as possible, and to minimize the relative size of the experimental errors.

Three key factors controlling the strain sensitivity of the hole-drilling method are the diameter and geometry of the hole and the geometry of the strain gauge rosette. The strain sensitivity of the hole-drilling method depends directly on the size of the hole relative to the rosette size. Maximum sensitivity for a given rosette size is achieved when the hole has the maximum allowable size. This maximum size is determined by the distance between the edge of the hole and the strain gauge grids. Unfortunately, even with maximum size hole, the sensitivity of the hole-drilling method is not very high. This modest sensitivity means that small strain measurement errors can cause significant errors in the calculated residual stresses. Two methods are proposed here to improve strain sensitivity and stress calculation accuracy: taper hole drilling and a modified design for the rosette.

Taper hole drilling improves the sensitivity of the hole drilling method by increasing the hole size without exceeding the limit for hole radius at the surface of the specimen. In this method, a truncated cone shape hole is drilled instead of a conventional cylindrical hole. By modifying the geometry of the hole, the effective size of the hole and the flexibility of the material in the region close to the hole are increased. This increase in flexibility of the material causes larger strain reliefs and improved sensitivity. This thesis describes and explains the sensitivity improvement that is achieved by tapered hole drilling. A practical drilling procedure is also briefly described. Experimental measurement of the sensitivity is compared with numerical results.

The geometrical design of the strain gauge rosette is the third key factor which influences the sensitivity of the method and its stress calculation accuracy. The ASTM standard hole-drilling rosette [8] is the most commonly used design, and is almost universal in North America. The pattern derives from the original 1966 work of Rendler and Vigness [7]. These two pioneering researchers do not give much detail concerning their choice of rosette geometry. One can speculate that theirs was a pragmatic choice between strain sensitivity and available strain gauge shapes. Certainly, their final selection has served well over many years. However, the more recent requirements for improved strain measurement accuracy for non-uniform stress evaluations heavily tax the capabilities of their rosette design.

This thesis examines how various rosette design factors contribute to overall strain sensitivity. It compares four different potential rosette geometries, and suggests an improved design that has an effective strain sensitivity almost three times greater than the present the ASTM standard pattern. The non-uniform stress calculations associated with the proposed rosette patterns are also numerically less sensitive than those for the ASTM design. Non-uniform residual stress profiles can be determined to depths about 25% greater than previously. Furthermore, the proposed pattern includes thermal strain

compensation, so the absolute sizes of the strain measurement errors are also reduced. A series of experiments was undertaken using the proposed strain gauge pattern, and the various features of the design were successfully demonstrated.

CHAPTER 2

THE HOLE DRILLING METHOD

2.1 Background Theory

The hole drilling method involves drilling a small hole into the stressed material. A specially designed strain gauge rosette measures the associated strain reliefs in the surrounding material [7,8]. Figure 2 shows a typical hole geometry. The residual stresses originally existing at the hole location can then be evaluated from the measured strains. In most hole-drilling measurements, it is assumed that the stresses in the specimen material are uniform with depth from the surface. However, in recent years, considerable interest has arisen for using the hole-drilling method to determine residual stresses that vary with depth from the specimen surface. Both cases are discussed in this thesis.

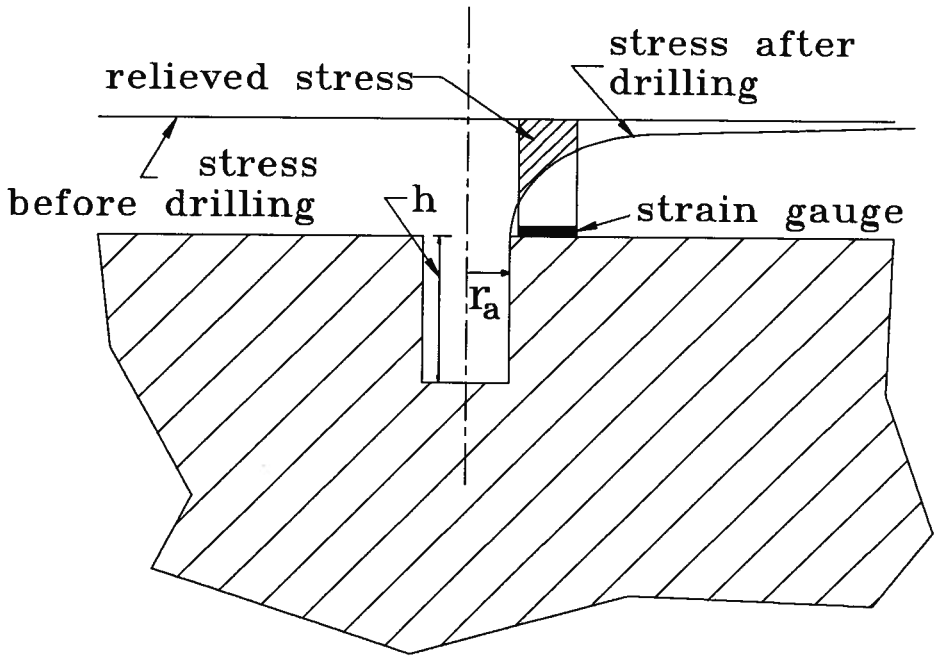

Figure 2 A typical hole geometry.

2.1.1 Uniform Residual Stress

When the residual stresses in a specimen do not vary with depth from the surface, the relationship between the measured relieved strains after the hole drilling and original existing residual stresses is of the form [7]:

$$\varepsilon = \overline{A}\,(\sigma_{max} + \sigma_{min}) + \overline{B}\,(\sigma_{max} - \sigma_{min})\cos 2\varphi \qquad (1)$$

where

ε = relieved strain measured by the strain gauge

σ_{max} = maximum principal residual stress

σ_{min} = minimum principal residual stress

φ = angular coordinate of the radial mid axis of the strain gauge measured counterclockwise from the maximum principal stress,

$\overline{A}, \overline{B}$ = calibration coefficients

The principal stresses and their orientations can be calculated by applying the above Equation for each of the strain gauges.

$$\sigma_{max}, \sigma_{min} = \frac{\varepsilon_1 + \varepsilon_3}{4\overline{A}} \mp \frac{((2\varepsilon_2 - \varepsilon_1 - \varepsilon_3)^2 + (\varepsilon_1 - \varepsilon_3)^2)^{1/2}}{4\overline{B}} \qquad (2)$$

$$\varphi = \frac{1}{2}\arctan\frac{2\varepsilon_2 - \varepsilon_1 - \varepsilon_3}{\varepsilon_1 - \varepsilon_3} \qquad (3)$$

where

$\varepsilon_1, \varepsilon_2$, and ε_3 = strains measured by the three strain gauges

φ = clockwise angle from gauge 1 to direction of σ_{max}

Numerical values of the calibration coefficients $\overline{A}$ and $\overline{B}$ must be known to determine residual stresses using Equation (2). For the idealized case of infinitesimal relieved radial strains around a through hole in a thin uniformly stressed plate the coefficients $\overline{A}$ and $\overline{B}$ can be determined analytically at a distance r from the hole radius as [2]:

$$A = -\frac{1+\nu}{2E}\left(\frac{r_a}{r}\right)^2 \tag{4}$$

$$B = -\frac{1+\nu}{2E}\left[\frac{4}{1+\nu}\left(\frac{r_a}{r}\right)^2 - 3\left(\frac{r_a}{r}\right)^4\right] \tag{5}$$

where r_a is the hole radius. In Equations (4) and (5), A and B are written without "bars" to emphasize that they refer to infinitesimal relieved strains. The corresponding infinitesimal A and B values for circumferential relieved strains are:

$$A = \frac{1+\nu}{2E}\left(\frac{r_a}{r}\right)^2 \tag{6}$$

$$B = \frac{1+\nu}{2E}\left[\frac{4\nu}{1+\nu}\left(\frac{r_a}{r}\right)^2 - 3\left(\frac{r_a}{r}\right)^4\right] \tag{7}$$

In the early years of the hole-drilling method, constants A and B from Equations (4) and (5) were sometimes used for hole-drilling residual stress calculations. However, this practice gives inferior results because practical relieved strain measurements occur over the entire areas of the strain gauges, not just at infinitesimally small areas. The values of

the calibration coefficients $\overline{A}$ and $\overline{B}$ can be calculated by integrating the values of A and B over the active areas of the strain gauges, [11].

In most cases, through holes are not practicable and blind holes must be used instead. When a blind hole is used, there are no convenient analytical values for the calibration coefficients $\overline{A}$ and $\overline{B}$. For this case, values of $\overline{A}$ and $\overline{B}$ are obtained either experimentally or numerically.

In experimental evaluation of the calibration coefficients [7, 8], a separate sample of the specimen material is used. A strain gauge rosette identical to actual residual stress measurement is installed on the sample surface. A hole with same geometry as the hole in actual residual stress measurement is drilled into this sample. By subjecting the sample to a known uniform stress field and by measuring the strains before and after the hole drilling, the calibration coefficients can be determined. The experimental calibration has the advantages of conceptual simplicity and accounting for the procedural influences and material-dependent effects on measured strain response. One disadvantage is that a separate time consuming calibration is needed for every material, hole size, and rosette geometry.

Numerical determination of the calibration coefficients $\overline{A}$ and $\overline{B}$ was made possible by the development of the finite element method [11]. Numerical calibration is more general and covers a wide range of measurement conditions. Numerical calibration closely matches the experimental calibration, and is widely accepted and used.

Figure 3 schematically shows the state of stress in a specimen both before and after hole-drilling. Figure 3(a) shows the stresses before hole drilling, including the stresses that exist at the boundary of the hole which is about to be drilled. Figure 3(b) shows the stresses after the hole drilling. The far boundary is assumed to be sufficiently distant that the stresses there are unaffected by the hole drilling. Figure 3(c), which shows the stress

difference between Figure 3(a) and Figure 3(b), represent the stress and strain redistribution caused by hole drilling. An analysis of the state of stress in Figure 3(c) directly gives the strain reliefs measured after hole drilling. The state of stress of Figure 3(c) can be modeled by the finite element method to determine the displacement field in the area surrounding the hole. This displacement field can be numerically integrated over the active strain gauge area to simulate the measured relieved strains [13]. Substituting these calculated strains and known stresses in Equation (1) yield the calibration coefficients $\overline{A}$ and $\overline{B}$.

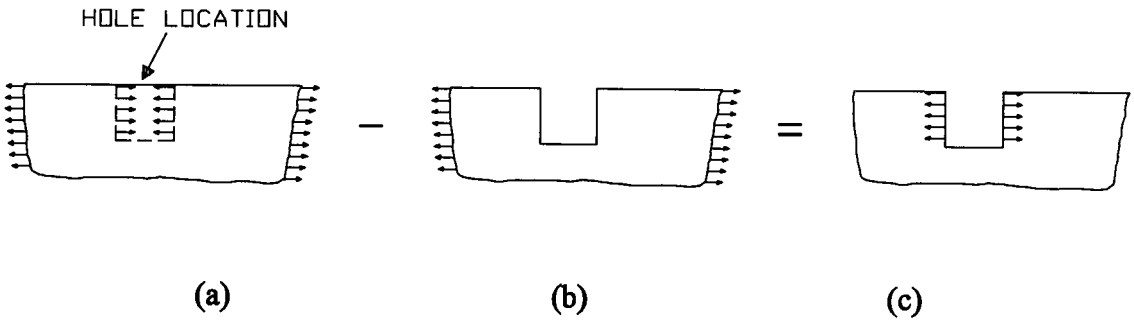

Figure 3 Stress distribution before and after the hole drilling.

Numerical calculations for each of the calibration coefficients $\overline{A}$ and $\overline{B}$ are done separately. In this way by applying a hydrostatic stress $\sigma_{max} = \sigma_{min} = 1$ coefficient $\overline{A}$ can be evaluated from Equation (1).

$$\overline{A} = \frac{\varepsilon_h}{2} \tag{8}$$

where ε_h is average strain (over the strain gauge grid) due to hydrostatic stress. Similarly $\overline{B}$ can be calculated as

$$\overline{B} = \frac{\varepsilon_s}{2\cos 2\varphi} \tag{9}$$

where ε_s is the average strain due to shear stress ($\sigma_{max} = -\sigma_{min} = 1$) and φ is the angle between the strain gauge mid radial axis and the principal stress direction.

The numerical values of the calibration coefficients depend on the hole diameter, hole depth, geometry of the strain gauge rosette, and the specimen material properties, Young modulus E and Poisson's ratio ν. The material property dependency can be mostly eliminated by introducing two dimensionless calibration coefficients $\bar{a}$ and $\bar{b}$ [11]:

$$\bar{a} = \frac{2E\overline{A}}{1+\nu} \qquad \bar{b} = 2E\overline{B} \tag{10}$$

In terms of these two constants, Equations (1) and (2) become

$$\varepsilon = \frac{(1+\nu)\,\bar{a}}{E}\,\frac{(\sigma_{max}+\sigma_{min})}{2} + \frac{\bar{b}}{E}\,\frac{(\sigma_{max}-\sigma_{min})}{2}\cos 2\varphi \tag{11}$$

$$\sigma_{max}, \sigma_{min} = \frac{E}{(1+\nu)}\frac{(\varepsilon_1+\varepsilon_3)}{2\bar{a}} \mp \frac{E\left((2\varepsilon_2-\varepsilon_1-\varepsilon_3)^2+(\varepsilon_1-\varepsilon_3)^2\right)^{1/2}}{2\bar{b}} \tag{12}$$

Further non-dimensionalization is effective in simplifying the hole radius and depth dependencies. Normalizing these two quantities with respect to the mean radius, r_m, of the strain gauge rosette make the calibration coefficients $\bar{a}$ and $\bar{b}$ (or $\bar{A}$ and $\bar{B}$) approximately proportional to the square of the normalized hole radius [11]. Figure 4 shows the variation of $\bar{a}$ and $\bar{b}$ with normalized hole depth for a normalized hole radius of r/r_m=0.5 [11]. The corresponding values of $\bar{A}$ and $\bar{B}$ for a given material can be evaluated through Equation (10). The numerical values of the calibration coefficients, then, can be substituted in Equation (2) to evaluate the residual stresses.

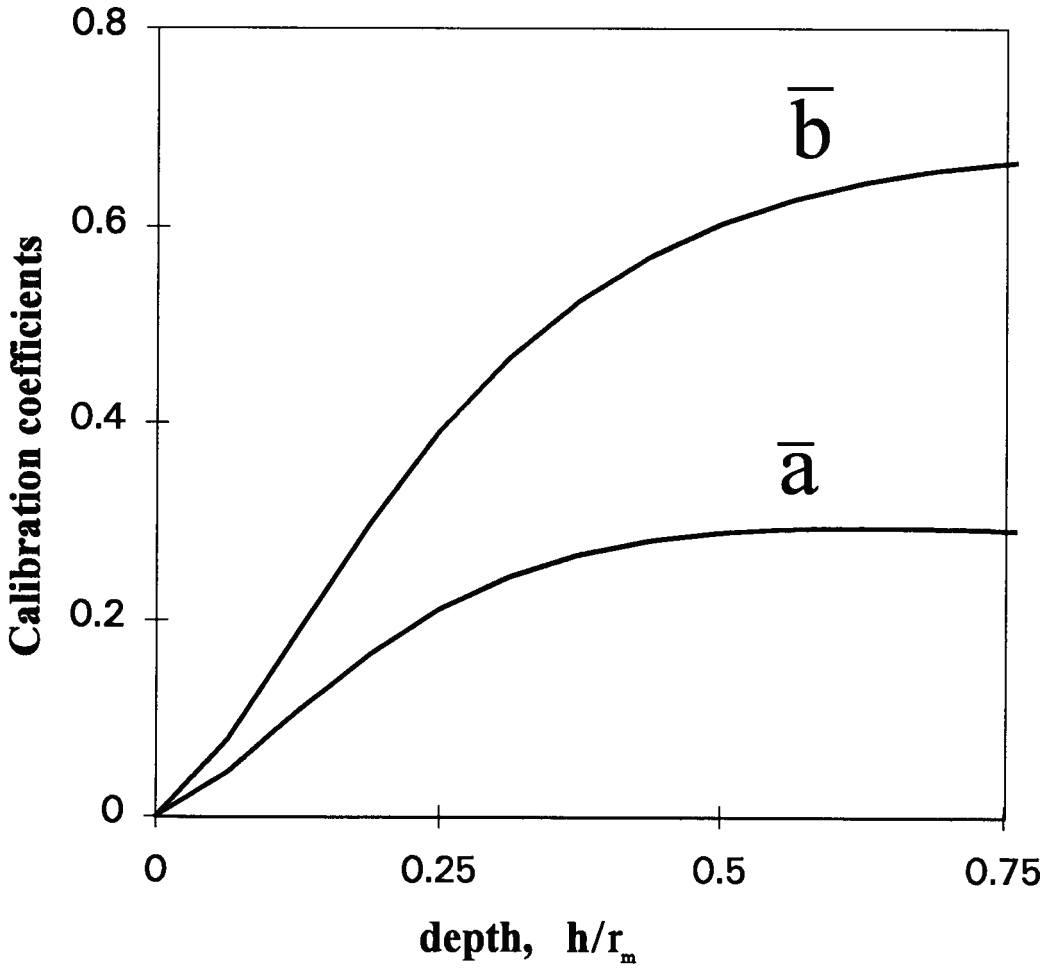

Figure 4 Calibration coefficients for $r_a/r_m = 0.5$.

2.1.2 Non-Uniform Residual Stress

The assumption that the residual stresses do not vary with depth is not always valid. In many practical cases the residual stress fields are significantly non-uniform. Processes such as shot peening, plating, and heavy grinding induce non-uniform stresses.

In measurement of the non-uniform residual stress field by the hole-drilling method, relieved strains are measured after drilling of several successive small increments of hole depth [12, 14, 15]. The analysis of the variation of these measured relieved strains with depth can be used to determine the original non-uniform stress field. There are a few stress calculation methods. Among these methods the Integral method probably is the most general [12].

The basis for the Integral method is that the strains measured during hole drilling are the cumulative result of relieving the residual stresses originally existing at all depth locations within the total hole depth. The individual contributions of the stresses at each depth location to the total measured strains are identified and the individual stresses are calculated from these total strain measurements [12, 14].

The method involves drilling the hole incrementally. The residual stresses are assumed constant within each increment. The total measured strain is the sum of the strains caused by relieving the residual stresses originally existing with each of the hole depth increments:

$$\varepsilon_i = \sum_{j=1}^{j=i} \left[\frac{(1+\nu)\,\bar{a}_{ij}}{E} \frac{(\sigma_{maxj} + \sigma_{minj})}{2} + \frac{\bar{b}_{ij}}{E} \frac{(\sigma_{max\,j} - \sigma_{min\,j})}{2} \cos 2\varphi_j \right] \quad (13)$$

where

ε_i = total measured relieved strain for i increments deep hole

$\sigma_{max\,j}$ = maximum principal residual stress at the increment j

$\sigma_{min\,j}$ = minimum principal residual stress at the increment j

φ_j = angular coordinate of the radial mid axis of the strain gauge measured counterclockwise from the maximum principal stresses at j increment

$\bar{a}_{ij}, \bar{b}_{ij}$ = calibration coefficients for j increment within a hole i increments deep

The individual calibration coefficients $\bar{a}_{ij}$ and $\bar{b}_{ij}$ relate the original existing residual stresses and relieved strains.

Equation (13) can be written in matrix form as

$$\{\varepsilon\} = \frac{(1+\nu)}{2E}[\bar{a}]\{\sigma_{maxj}+\sigma_{minj}\} + \frac{1}{2E}[\bar{b}]\{(\sigma_{maxj}-\sigma_{minj})\cos 2\varphi\} \quad (14)$$

where $\{\varepsilon\}$ is a vector of the strain reliefs measured at series of hole depth increments from the hole surface. The corresponding stress vectors contain the principal stress quantities and directions within each hole depth increment. The calibration coefficients $[\bar{a}]$ and $[\bar{b}]$ become matrix quantities with a lower triangular structure [12]:

$$[\bar{a}] = \begin{bmatrix} \bar{a}_{11} & & & \\ \bar{a}_{21} & \bar{a}_{22} & & \\ \bar{a}_{31} & \bar{a}_{32} & \bar{a}_{33} & \\ . & . & . & . \end{bmatrix} \qquad [\bar{b}] = \begin{bmatrix} \bar{b}_{11} & & & \\ \bar{b}_{21} & \bar{b}_{22} & & \\ \bar{b}_{31} & \bar{b}_{32} & \bar{b}_{33} & \\ . & . & . & . \end{bmatrix} \quad (15)$$

Conceptually the stress within each increment can be calculated from the measured stress $\{\varepsilon\}$ by solving the matrix Equation (14). This equation is non-linear, and stress solutions are usually found in practice using a linear reformulation, [12, 15]. The values of the individual coefficients $\bar{a}_{ij}$ and $\bar{b}_{ij}$ depend on the width position of increment j and the total depth and diameter of the hole. Figure 5 shows a physical interpretation of the

calibration coefficients $\bar{a}_{ij}$. The same interpretation applies for $\bar{b}_{ij}$. The columns of the matrices $[\bar{a}]$ and $[\bar{b}]$ correspond to the relieved strains caused by the stresses within a fixed increment for holes of increasing depth. The increasing hole depth causes these individual coefficients to increase within each column. The rows of the matrices correspond to the relieved strains caused by stresses within successive increments of a hole of fixed depth. The sum of all the coefficients in each row corresponds to a uniform stress field over the entire depth, i.e., $\bar{a}$ and $\bar{b}$ in Equation (11).

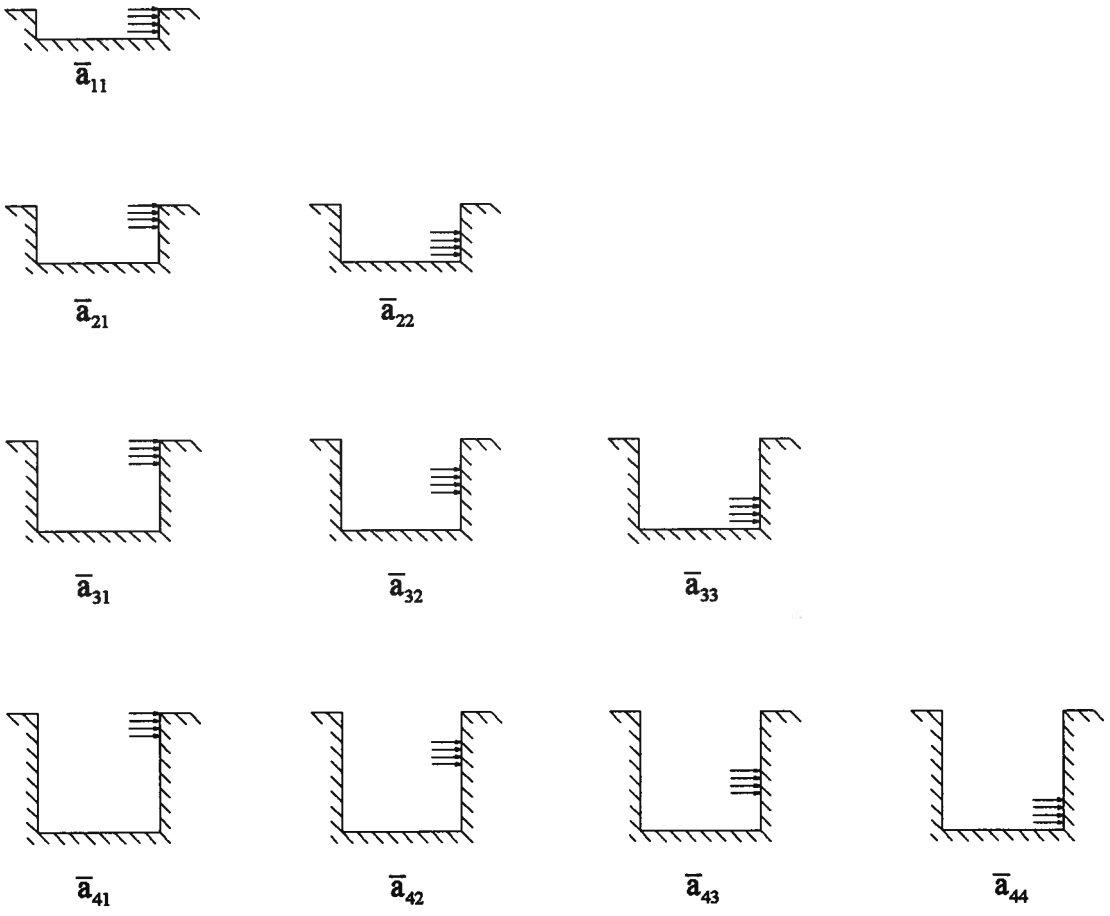

Figure 5 Stress loadings corresponding to calibration coefficients $\bar{a}_{ij}$.

In practice, it is very difficult to produce layered stress fields of the type shown in Figure 5. Thus, the calibration coefficients matrices $[\bar{a}]$ and $[\bar{b}]$ are not determined experimentally. Finite element calculation, however, provides a very effective and reliable method for evaluating these coefficients. A full description of such calculations is given by Schajer [12].

2.2 Strain Sensitivity of the Hole-drilling Method

The strain sensitivity of the hole-drilling method is typically quite modest. A low strain sensitivity can diminish the reliability of the calculated residual stresses by reducing the size of the measured strains relative to that of the strain measurement errors. The strain sensitivity, defined as the relieved strain per unit residual stress, is quantified through the calibration coefficients $\bar{a}$ and $\bar{b}$. Larger calibration coefficients are desirable because they indicate higher strain sensitivity, and hence greater resistance to the effects of strain measurement errors.

The values of $\bar{a}$ and $\bar{b}$ (or $\bar{A}$ and $\bar{B}$) are low because the strain gauges are located at some distance from the hole. The material underneath the gauges is subjected only to partial strain relief. If it were possible to relieve completely the strains in the material under all the gauges, then it may be shown from Hooke's Law that the corresponding calibration coefficients would be:

$$\begin{aligned} &\text{maximum value of } \bar{a} = \frac{1-\nu}{1+\nu} = 0.54 \quad \text{for } \nu = 0.3 \\ &\text{maximum value of } \bar{b} = 1+\nu = 1.3 \quad \text{for } \nu = 0.3 \end{aligned} \tag{16}$$

Figure 4 shows that for the traditional straight hole, the maximum values of $\bar{a}$ and $\bar{b}$ are at most only half of the full strain relief values. Thus, significant scope exists for increasing the strain sensitivity of the strain measurements.

Stress calculation accuracy is an additional major concern when using Equation (14) to determine the profile of residual stresses with respect to depth [12, 16]. The matrix quantities $[\bar{a}]$ and $[\bar{b}]$ become poorly conditioned numerically at larger depths. This effect causes the calculated stresses at greater depths from the specimen surface to be much more prone to error than the stresses at the lesser depth. This error sensitivity can be quantified through condition numbers of the matrices $[\bar{a}]$ and $[\bar{b}]$. A simple approximation is given in [12] as :

$$C_{Ai} = \frac{\bar{a}_i}{\bar{a}_{ii}} \quad \text{and} \quad C_{Bi} = \frac{\bar{b}_i}{\bar{b}_{ii}} \tag{17}$$

where C_{Ai} and C_{Bi} are the condition numbers of matrices $[\bar{a}]$ and $[\bar{b}]$ for stress calculations at increment i. The quantities $\bar{a}_i$ and $\bar{b}_i$ are the $\bar{a}$ and $\bar{b}$ values corresponding to a hole i increments deep in a uniform stress field. Their numerical values are:

$$\bar{a}_i = \sum_{j=1}^{i} \bar{a}_{ij} \qquad \bar{b}_i = \sum_{j=1}^{i} \bar{b}_{ij} \tag{18}$$

The condition numbers C_{Ai} and C_{Bi} indicate the percent stress calculation errors for the ith increment caused by one percent strain measurement error within the same increment. The larger the condition numbers, the greater is the influence of strain measurement errors on the computed residual stresses.

Strain sensitivity and matrix numerical conditioning both control how strain measurement errors influence the calculated residual stresses. High strain sensitivity and

low condition numbers are desirable to reduce stress calculation error. These two effects can be combined into stress evaluation reliability factors defined as:

$$F_{Ai} = \frac{\bar{a}_i}{C_{Ai}} \quad \text{and} \quad F_{Bi} = \frac{\bar{b}_i}{C_{Bi}} \tag{19}$$

High values of these factors indicate reduced influence of strain measurement errors.

Hole size and rosette geometry both strongly influence the reliability factors. Hole size mainly affects the strain sensitivity. Rosette geometry affects both strain sensitivity and condition numbers. The objective of this study is to improve both the strain sensitivity and numerical conditioning of hole drilling method. This objective will be approached in two ways. The first way will be to modify the shape and size of the drilled hole. The second way will be to modify the geometry of the strain gauge rosette. This study will concentrate on the effect of these two factors, and how they can be affected to produce beneficial results.

CHAPTER 3

TAPER HOLE DRILLING

The strain sensitivity of the hole-drilling method increases with the increasing size of the hole relative to the rosette size. The maximum allowable size is determined by the distance between the edge of the hole and the strain gauge grids. However, this hole size limit is not quite as restrictive as it may appear. The limitation applies strictly only to that part of the hole that intersects the specimen surface. By drilling a reverse tapered hole as shown in Figure 6, instead of a straight hole it is possible to increase the effective size while maintaining the hole size limit of the surface. More stressed material is removed close to the measurement area and more strain is relieved locally.

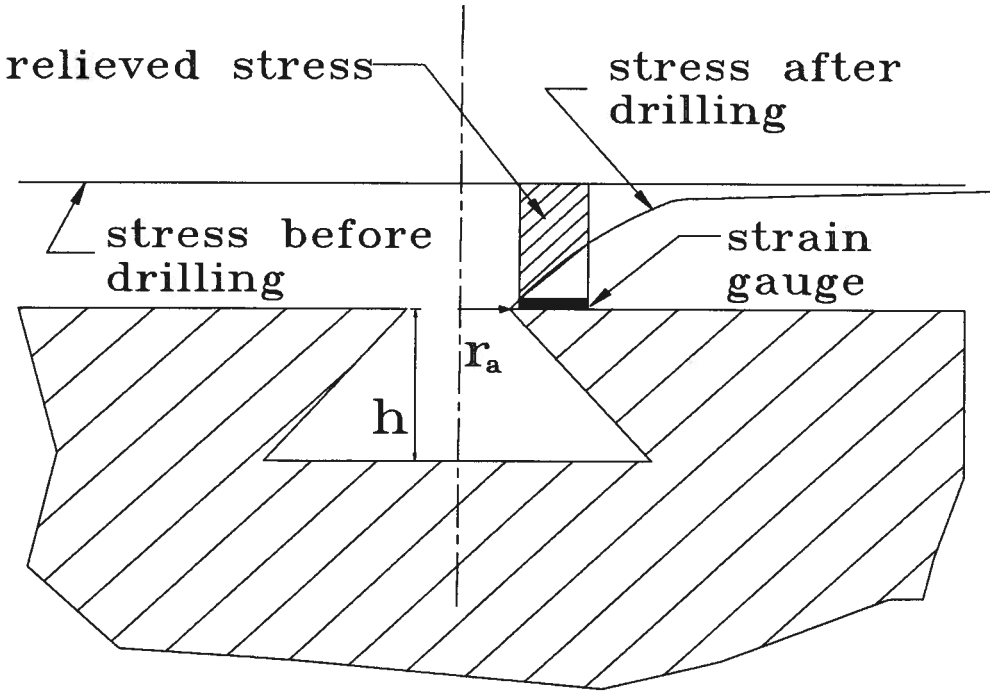

Figure 6 Cross section of a taper hole.

3.1 Drilling a Taper Hole

A reverse taper hole can be cut using an inverted cone drill bit in a high-speed air-turbine drive. Figure 7 shows a photograph of the jig that was designed to drill reverse taper holes for this study. Figure 8a shows a schematic cross-section of the drilling jig used in this study. A high-speed air turbine drive "A" mounts inside an upper slide "C", secured by a vertical height adjustment micrometer "B". A diagonal motion, at 50° to the horizontal, is provided by a dovetail slider "D", and is controlled by a micrometer "I". The slider is secured to the working specimen "H" through a ball bearing "E". The bearing has a split inner ring to eliminate any free play. An inverted cone drill bit "G", shown in detail in Figure 8b, mounts at the lower end of the high speed air turbine "A".

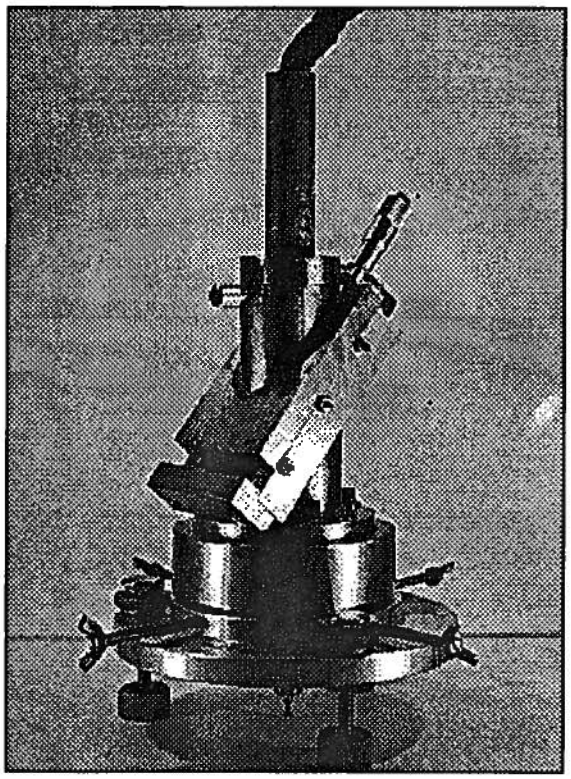

Figure 7 Photograph of the taper hole drilling jig.

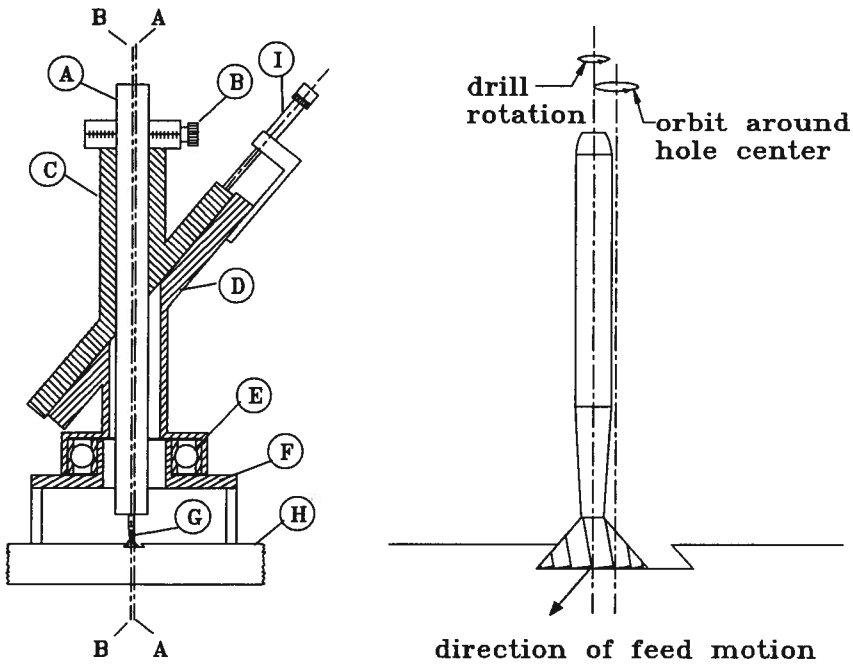

Figure 8 Taper hole drilling device: (a) = cross-section; (b) = detail of drill bit; A = high speed turbine; B = height adjustment micrometer; C = upper slide tube; D = lower slider; E = ball bearing, F = base; G = inverted cone drill bit; H = specimen; I = diagonal micrometer; A-A = fixed central axis; B-B = drilling axis.

The taper drilling procedure starts by adjusting the diagonal adjustment micrometer so that the air turbine "A" and the drill bit "G" are centered relative to the ball bearing "E" (axis A-A). The vertical height micrometer "B" is then adjusted so that the drill bit "G" just touches the surface of the specimen "H". Drilling proceeds by incrementally lowering the diagonal micrometer "I", causing the drill bit to move diagonally downward. The diagonal motion displaces the relative axis of the drill bit from A-A to B-B. Rotation of the bearing "E" causes the drill bit axis B-B to orbit around the fixed axis A-A, thus creating a reverse taper hole. This hole can be enlarged by further lowering of the upper slide by the diagonal micrometer "I" and repeated orbiting by rotating the bearing "E".

After drilling, the surface diameter of the taper hole must be measured. Conventional measurement tools are not suited to measure the diameter of small taper holes. An electronic vernier caliper was modified by silver soldering two 2.4 mm diameter balls to the tips of the caliper fingers, as shown in Figure 9. The caliper measures the distance between the balls when the balls touch the perimeter and the bottom surface of the taper hole. The surface diameter of a taper hole can then be calculated from the distance between the balls and depth of the hole.

To confirm the reliability of the modified caliper, eight sample taper holes were drilled. A caliper measurement was made on each hole, from which the surface diameter was calculated. Typical surface diameters were in the range 5.8-6.1 mm. Then, surface diameters were measured in a different way. Each hole specimen was sectioned so that a diameter of the hole was exposed. The surface diameter was then measured optically using a traveling microscope. Figure 10 shows a cross-section of a typical taper hole. The root mean square difference between the surface diameter measurements from the two methods was found to be 0.03 mm.

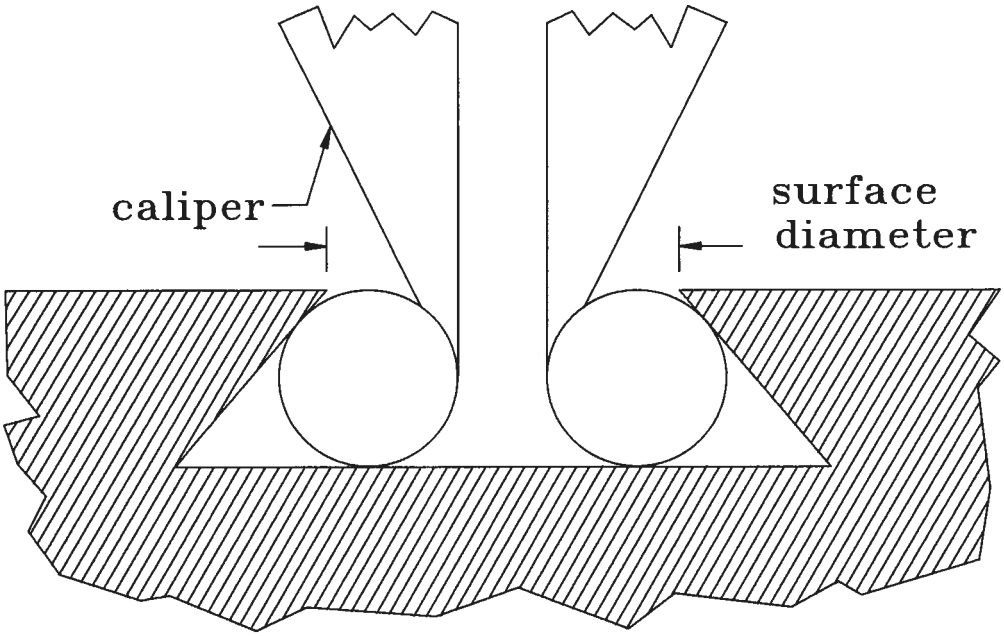

Figure 9 Measurement of taper hole diameter by a modified caliper.

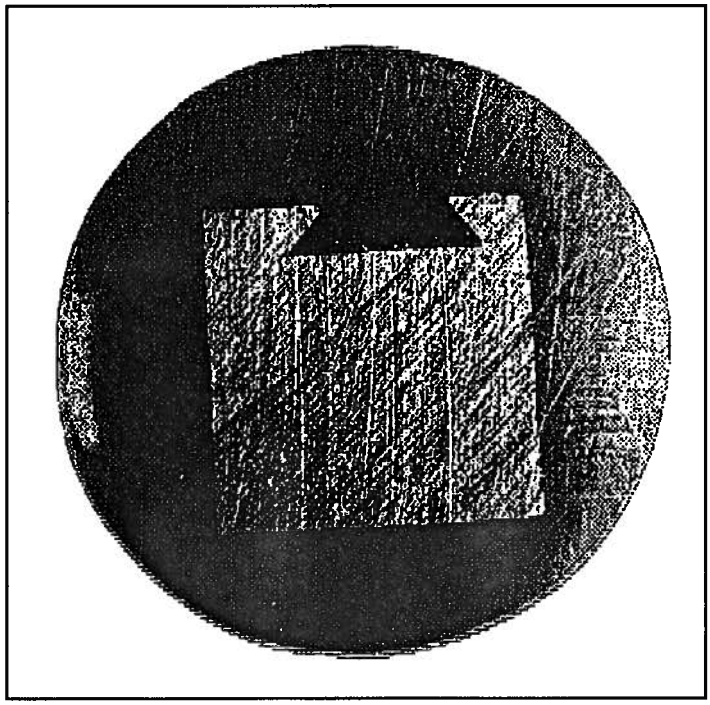

Figure 10 A cross-section of a sample drilled taper hole.

3.2 Taper Hole Calibration Coefficients

Equations (11) and (1) still apply to taper hole drilling. However, the numerical values of the calibration coefficients $\bar{a}$ and $\bar{b}$ (or $\bar{A}$ and $\bar{B}$) are larger than when drilling a straight hole. They can be evaluated, as in the case of a straight hole, either by experiment or by numerical calculation.

The numerical procedure for determining $\bar{a}$ and $\bar{b}$ for a taper hole by finite element calculation is similar to the calculation for the case of a straight hole. As shown in [11], the strain reliefs caused by hole drilling correspond to the strains induced by applying stresses to the hole boundaries which are equal in magnitude but opposite in sign to the existing residual stresses. The surface displacements caused by this loading are calculated using the finite element method. The strains over the strain gauge area can then be directly determined from the surface displacements [13].

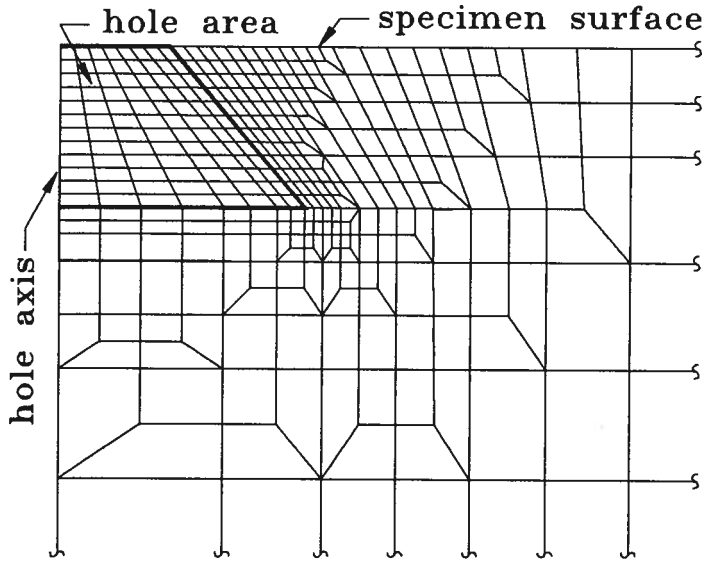

Figure 11 Detail of the finite element mesh for a tapered hole.

A finite element mesh of 432 nodes and 396 elements was used for the calculation. Figure 11 shows the portion of the mesh for the area around the hole. The depth of the hole is adjusted during the various calculations by assigning a near zero elastic modulus to the elements within the required hole depth. Figure 12 shows a result of these calculations, a graph of the calibration coefficients $\bar{a}$ and $\bar{b}$, for the taper hole case. For comparison, Figure 12 also shows calibration coefficients for the straight hole case.

As can be seen, the calibration coefficients for taper hole drilling compare favorably in two different aspects with their corresponding straight hole values; they are larger in magnitude, and have their peaks at shallower depths. These two features allow greater measurement accuracy to be achieved while causing less damage to the specimen.

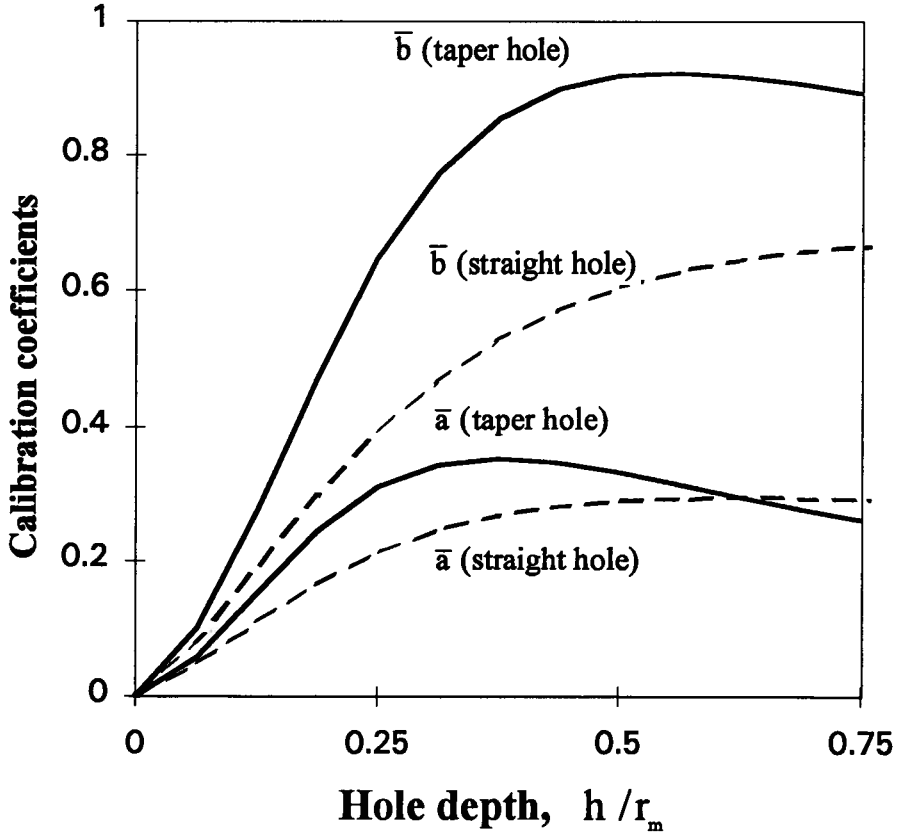

Figure 12 Theoretical calibration coefficients for straight and tapered holes for $r_a/r_m = 0.5$.

Figure 13 explains the reason for these favorable changes. The figure shows exaggerated views of the displaced shapes around a straight hole and a taper hole subjected to a unit biaxial stress field. In the taper hole case, the displacements are generally much larger than those of the straight hole case. This feature implies that the taper hole drilling more effectively relieves the residual stresses around the hole, and that the remaining adjacent material is more flexible than in the straight hole case. These factors combine to increase the rate of strain relief during taper hole drilling, i.e., the increase in initial slopes of the curves in Figure 12. Maximum strain reliefs are also reached sooner, so that the peaks of the curves for taper holes in Figure 12 occur at smaller depths than those for straight holes.

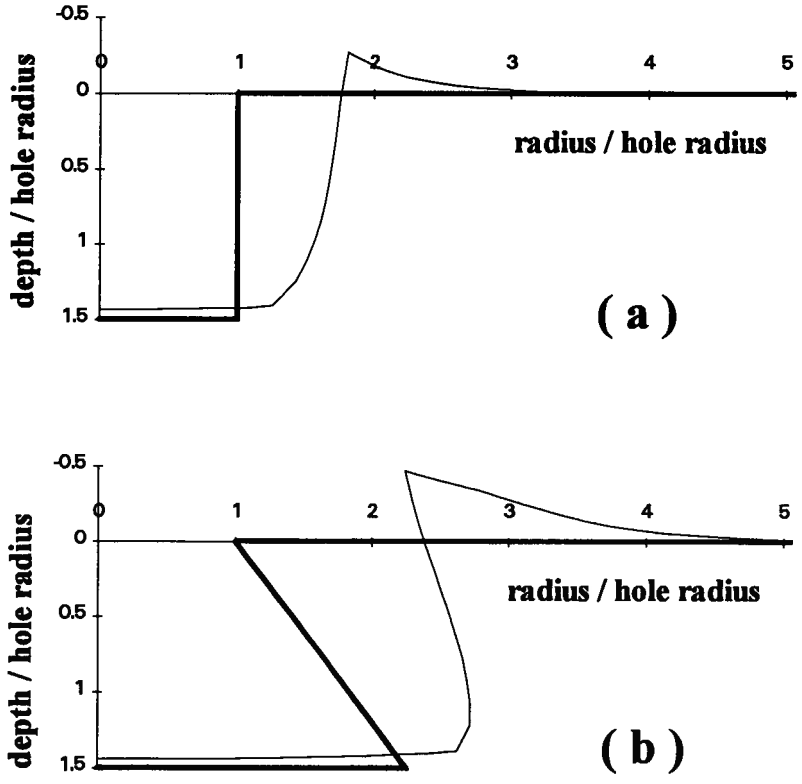

Figure 13 Exaggerated displaced shape profile of straight and tapered holes.
(a) straight hole (b) taper hole

3.3 Experimental Verification

Experiments were conducted to verify the theoretical results in Figure 12. The experiments had three objectives: (1) to determine how well the finite element calculations can predict the actual $\bar{a}$ and $\bar{b}$ values measured experimentally, (2) to compare the experimental calibration coefficients for straight hole and taper holes, (3) to demonstrate the practicality of using taper holes for hole-drilling residual stress measurements.

Two 125-RE strain gauge rosettes were installed on a 12.7 x 38.1 x 565 mm aluminum bar sample shown in Figure 14. Two additional single strain gauges were installed on the sides of the sample to monitor any bending loads. Undesirable bending strains were minimized by applying the loads through loading pins inserted through holes drilled at each end of the sample. The additional strain gauges mounted on the side faces of the test sample confirmed that bending strains, both within and out of plane, were less

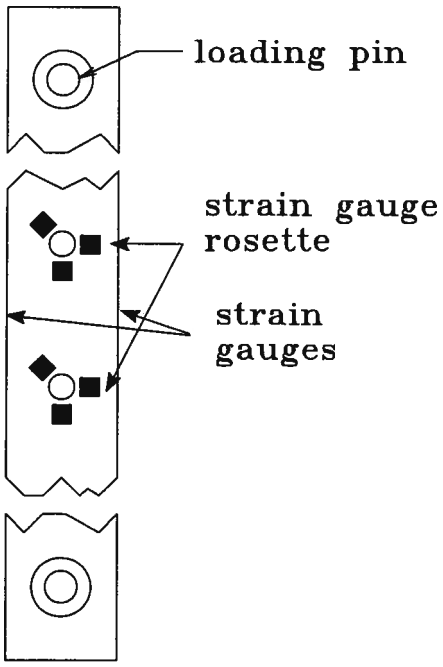

Figure 14 Tension test sample.

than 2% of the tensile strain. The sample was subjected to a range of tensile loads from zero to 35 kN in 7 kN increments, and the corresponding strains were recorded. The measured response of the strain gauges per unit load was determined from the gradient of the strain versus load plots. This procedure reduces the effect of random strain measurement errors and of any existing residual stresses.

A taper hole was drilled into the material at the center of the strain gauge rosette in four consecutive 0.58 mm depth increments. Drilling was done by the device described in Section 3.1. After drilling each increment, the sample was subjected to the same range of loads and the corresponding strains were recorded. Again, the response of the strain gauges per unit applied load was determined from the gradient of the strain versus load plots. After the drilling, the surface diameter of the taper hole was measured as 5.79 mm. This corresponds to a normalized hole radius $r_a/r_m = 0.564$. From these data, the calibration coefficients $\bar{a}$ and $\bar{b}$ for a taper hole were evaluated using the method described by Rendler and Vigness [7]. To provide comparative results, the entire experimental procedure was repeated using conventional straight hole drilling, using a hole diameter of 5.72 mm corresponding to a value of $r_a/r_m = 0.557$.

Figure 15 compares the experimentally determined calibration coefficients $\bar{a}$ and $\bar{b}$ with the theoretical values from the finite element calculations. The results show excellent agreement between numerically calculated calibration coefficients and their values determined by experiment. The differences between experimental results and theoretical predictions are typically less than 2%, reaching to 3% only in extreme cases. The experimental results confirm the theoretical prediction that taper hole drilling significantly increases the strain sensitivity of the hole-drilling method. Also, strains are relieved more rapidly so that shallower holes can be used. The experimental work also

confirms the practicality of drilling reverse taper holes instead of the conventional straight holes using a drilling jig such as the one shown in Figure 8.

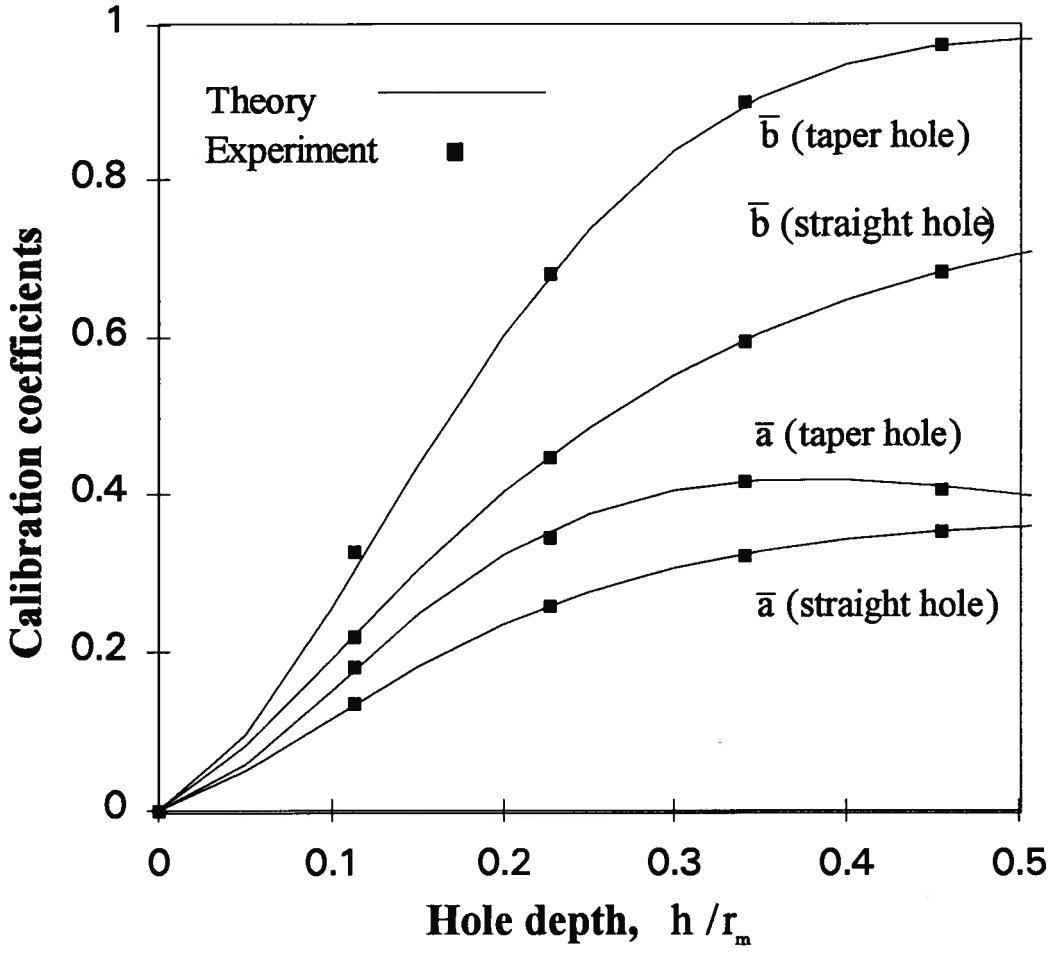

Figure 15 Comparison of experimentally measured calibration coefficients with theoretically predicted values.

CHAPTER 4

NEW STRAIN GAUGE GEOMETRY

The second key factor that affects the strain sensitivity of the hole-drilling method is rosette geometry. Rosette geometry also strongly influences the condition numbers (Section. 2.1.2). This chapter focuses on rosette geometrical design, and identifies features that lead to improved strain sensitivity and stress evaluation reliability factors.

4.1 Influence of strain gauge geometry on the calibration coefficients

The strain sensitivity of the hole drilling method is directly indicated by the calibration coefficients $\bar{a}$ and $\bar{b}$. However the effects of these calibration coefficients on stress calculation accuracy of the method are not equal. Because the calibration coefficient $\bar{a}$ has a smaller value than $\bar{b}$, it has a more detrimental influence on the stress calculation accuracy. This effect can be seen in Equation (12). The first term on the right side represents the isotropic (equal biaxial) stress component, and the second term represents the shear stress component. On average, these stress components have similar magnitudes. However, the value of $\bar{a}$ in the first term is much smaller than that of $\bar{b}$ in the second term. This difference makes the first stress term more sensitive to strain measurement errors than the second term. The calculated principal stress values combine the errors in both terms, particularly the larger error. Thus, for most effective stress calculation accuracy improvement, effort should be concentrated on increasing the value of $\bar{a}$, preferably so that it reaches the value of $\bar{b}$.

The length, the difference between inner and outer radii of the strain gauge, significantly influences strain sensitivity. This can be seen from the fact that the strains around the hole diminish rapidly with distance from the hole. Therefore, the smaller the

length of the strain gauge a greater fraction of the strain gauge will be in the high-strain region close to the hole.

Shorter strain gauge lengths enhance the numerical values of $\bar{a}$ and $\bar{b}$ significantly. However, a short gauge length can reduce the active area of the gauge and reduce its capacity as a heat sink. Such a gauge will be more susceptible to thermal drift. The active area of the strain gauges can be a measure of thermal stability of different strain gauge designs. For comparable thermal stability, the different strain gauge designs investigated in this study have equal active areas.

The other important geometrical factor that influences strain sensitivity is the orientation of grid lines of the strain gauges. To study the effects of this factor on the values $\bar{a}$ and $\bar{b}$, two new strain gauge designs with their grid lines oriented radially and circumferentially were studied. Comparison of these two designs with the existing rectangular design helped to design a more effective pattern for the strain gauge rosette. The active areas of these two new strain gauges were designed to be the same as the standard ASTM strain gauge. Figure 16 shows the radial strain gauge rosette and Figure 17 shows the circumferential rosette.

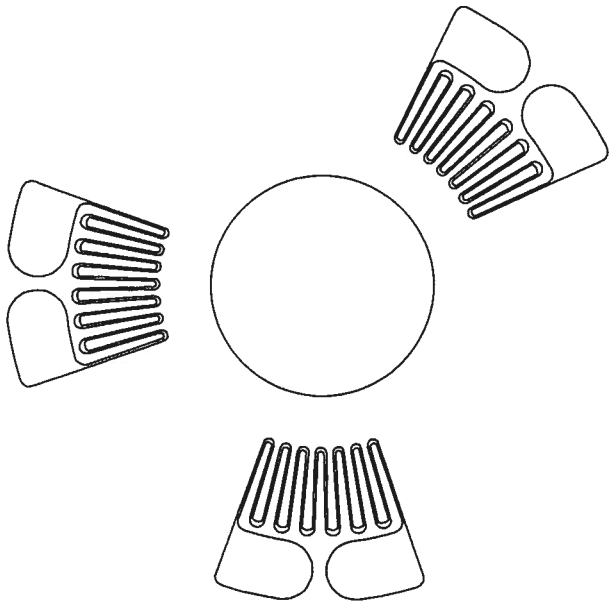

Figure 16 Radial strain gauge rosette.

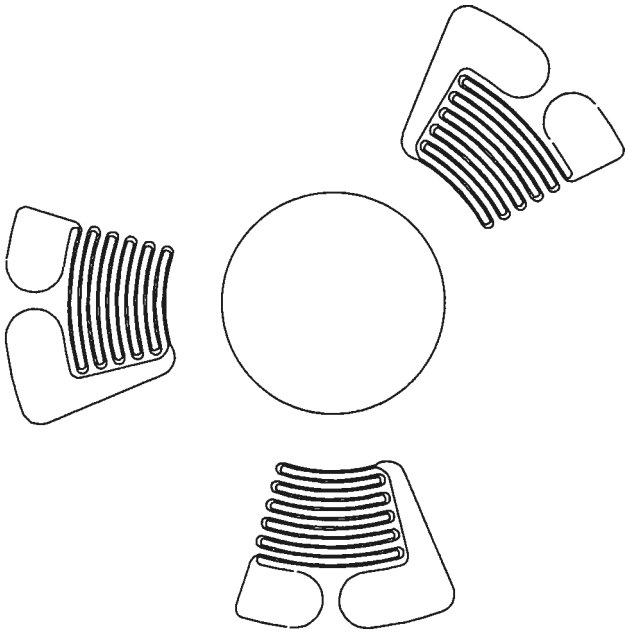

Figure 17 Circumferential strain gauge rosette.

4.2 Evaluation of calibration coefficients for different strain gauge geometries

To investigate the influence of strain gauge geometrical design on the numerical values and conditioning of the calibration coefficients the radial and circumferential strain gauge designs shown in Figures 16 and 17 were examined. For comparison a rectangular model, which has the same geometry as conventional ASTM strain gauge rosette shown in Figure 1 was also considered. The calibration coefficients, condition numbers and reliability factor for these strain gages for uniform and non-uniform stresses are calculated. The thickness and width of the strain gauge filaments are kept the same as the standard ASTM rosette. The active area of the strain gauge grid is the same as the standard rosette to maintain thermal stability. These strain gauges have the same inner radius as ASTM rosette so that the maximum allowable hole sizes are the same.

Calibration coefficients $\bar{a}$ and $\bar{b}$ were calculated by averaging the finite element calculated surface displacement data [13] over the strain gauge grid [11]. These displacement data are the same for each different strain gauge geometry; however, the required calculations are different for each different geometry.

For the calculation of average strain over the rectangular and radial strain gauge the following Equation, derived by Schajer [13], is used.

$$\varepsilon = \frac{\sum_i \frac{U_{2i} - U_{1i}}{w_i}}{\sum_i \frac{L_i}{w_i}} \tag{20}$$

where

U_{1i} and U_{2i} = displacements in the direction of the filament i at its two ends

L_i, w_i = length and width of the filament i

Equation (20) is only valid for straight line grids of uniform width and can be used in evaluation of strains for rectangular and radial strain gauge grids. Corresponding values of these strain reliefs can be used to evaluate calibration coefficients $\bar{a}$ and $\bar{b}$ from Equations (8), (9) and (10). The results of these calculations for rectangular and radial strain gauge are shown in Figure 18. Note that in this and subsequent graphs, the hole depth is normalized relative to the inner gauge radius, r_i, rather than the mean radius, r_m. This is done so that the graphs all refer to the same maximum hole size, independent of changes in strain gauge length.

Calculating $\bar{a}$ and $\bar{b}$ for a circumferential strain gauge needs a different analytical approach that is described in the appendix. The final results are given here.

$$\bar{a} = \frac{E}{(1+\nu)} \frac{\sum_i U_i}{\sum_i r_i} \quad \text{and} \quad \bar{b} = 2E \frac{\sum_i (U_i + 2V_i)}{\sum_i r_i} \frac{\sin\varphi}{\varphi} \tag{21}$$

where

U_i and V_i = radial and circumferential displacements at filament i

φ = grid angle of the strain gauge

r_i = mean radius of the filament i

Figure 18 also shows graphs of calibration coefficients for a circumferential strain gauge based on the above equations.

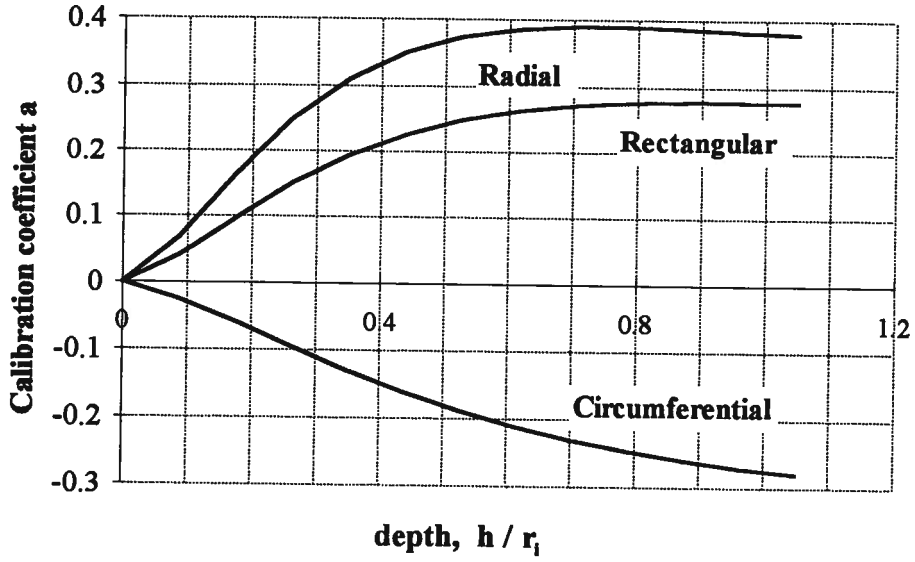

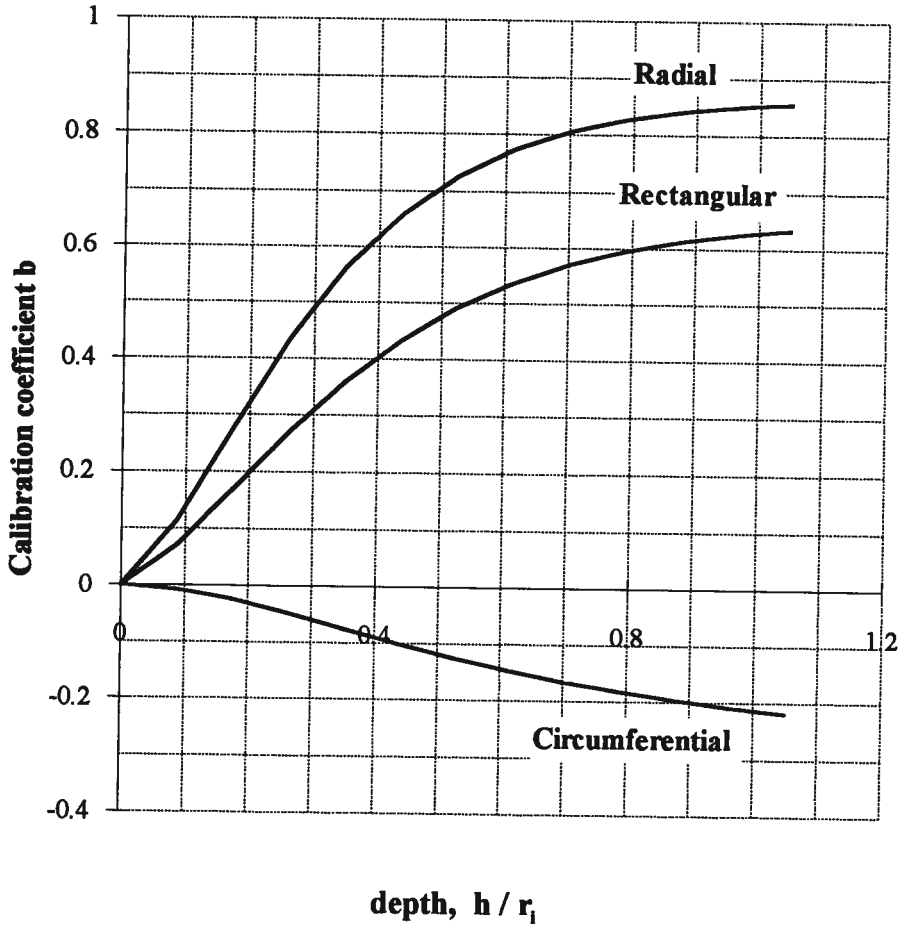

Figure 18 Calibration coefficients $\bar{a}$ and $\bar{b}$ for three different strain gauge designs.

4.3 Calibration coefficients for different strain gauge geometries

Figure 18 demonstrates that both calibration coefficients $\bar{a}$ and $\bar{b}$ are larger for a radial strain gauge than a rectangular one. On the other hand, the calibration coefficients for a circumferential strain gauge are smaller in magnitude than for a rectangular one. In addition the circumferential coefficients have the opposite sign relative to rectangular and radial strain gauge coefficients.

Calibration coefficient $\bar{a}$ for a radial strain gauge is increased by about 40 % and $\bar{b}$ by about 35 %. Two factors cause these improvements: (1) a larger fraction of the strain gauge area is in the high-strain region close to the hole boundary, due to the shorter length of the radial strain gauge relative to rectangular design. (2) by using radial filaments, the negative effect of the circumferential strain, which is present in the rectangular strain gauge grid, is eliminated. An additional advantage of using a radial strain gauge is that the calibration coefficient curves for this strain gauge reach their maximum values at a shallower depth compared with a rectangular strain gauge; therefore, a shallower hole needs to be drilled.

In contrast, a circumferential strain gauge provides smaller calibration coefficients than a rectangular strain gauge. These reductions in the values of calibration coefficients are due to the smaller circumferential strains around the hole area compared with the radial strains.

These results indicate that a radial strain gauge has higher strain sensitivity and is better suited to measuring a uniform stress field than the conventional ASTM strain gauge. However, the influence of these new designs on stress calculations for measuring non-uniform stress fields must also be studied.

The effects of the various strain gauges on calculations of the non-uniform residual stress fields can be examined by considering the condition numbers C_{Ai} and C_{Bi}. Figure 19 shows a graph of the inverse of these condition numbers, i.e., $1/C_{Ai}$ and $1/C_{Bi}$ versus increasing hole depth. Small inverse condition numbers indicate worse numerical conditioning and higher error. These graphs show that the effects of the different strain gauge geometries are not very significant for calibration coefficient $\bar{b}$. However for calibration coefficient $\bar{a}$ the circumferential strain gauge has the best inverse condition number and the radial one has the worst inverse condition number.

Figures 18 and 19 show that the radial strain gauge has higher strain sensitivity but poorer condition number and the circumferential strain gauge has lower strain sensitivity but better condition numbers. However, both the strain sensitivity and condition number affect the stress calculation errors due to strain measurement errors. Therefore, the effects of these factors must be considered together. The stress evaluation reliability factors F_{Ai} and F_{Bi} are defined in Section 2.2 for this purpose. Higher stress evaluation reliability factors indicate more reliable stress evaluations. Figure 20 shows the values of these reliability factors for the radial, circumferential, and rectangular strain gauge rosettes.

Figure 20 shows that the reliability factors for a radial strain gauge has larger values than for a rectangular one up to the depth $0.4r_i$ for F_{Ai} and up to depth $0.6r_i$ for F_{Bi}. However the rectangular strain gauge is reliable for measuring residual stresses up to depth $0.7r_i$ [12, 15, 16]. Therefore the radial strain gauge is useful only when residual stresses are within the $0.4r_i$ of the surface. In contrast, the circumferential strain gauge has larger values for F_{Ai} than the rectangular strain gauge for depths larger than $0.4r_i$. However the corresponding values F_{Bi} are very low.

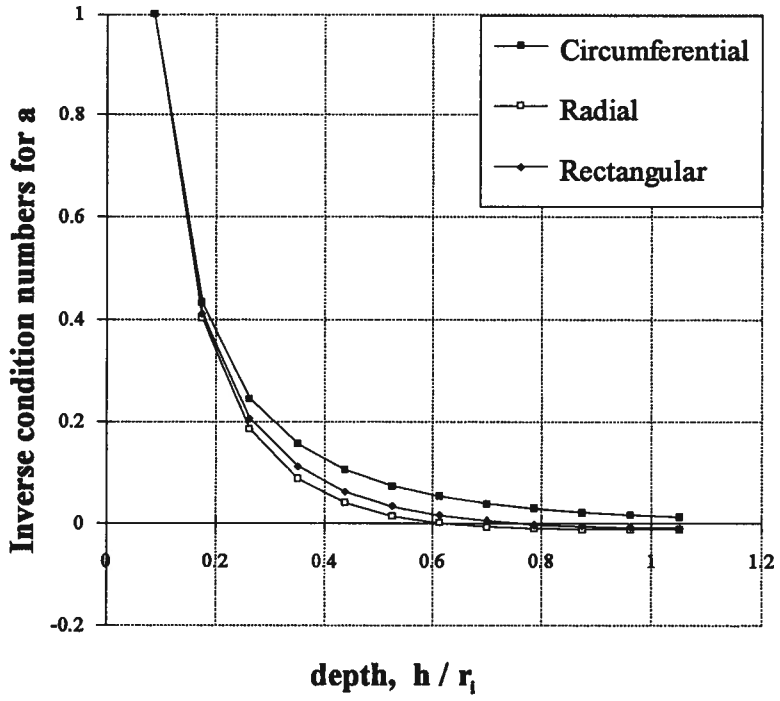

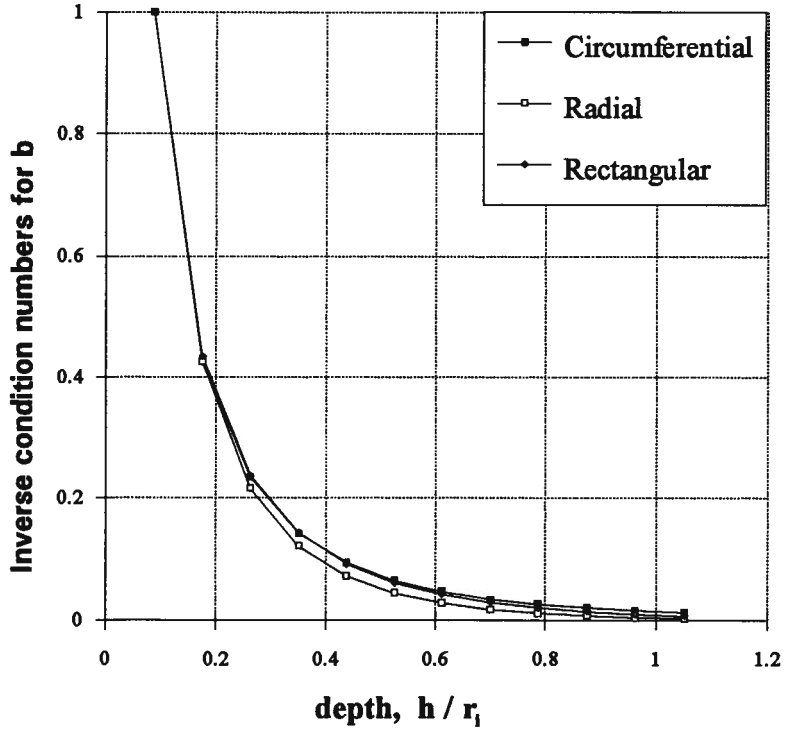

Figure 19 Inverse condition numbers for three different strain gauge designs.

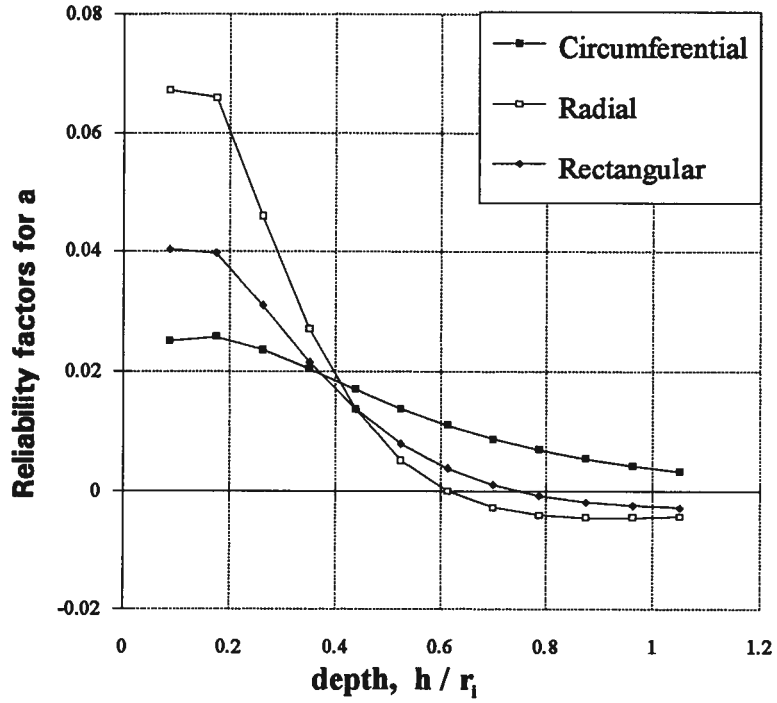

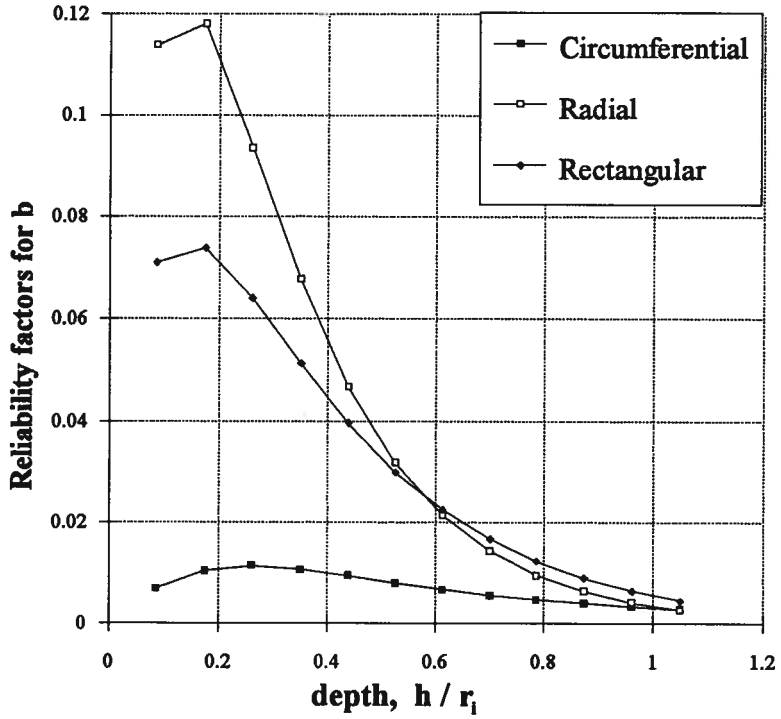

Figure 20 Reliability factors for three different strain gauge designs.

The above observations show that the radial and the circumferential strain gauge designs have opposite strengths and weaknesses. The radial design has higher sensitivity and the circumferential design has better non-uniform stress calculation stability. The strength of both designs can be combined by using a six-element rosette, as shown in Figure 21. This rosette has both radial and circumferential strain gauges. Each corresponding pair is connected in a half bridge circuit. This arrangement effectively adds the strains of two gauges together because the circumferential strains have the opposite sign to the radial strains. Greatly increased thermal stability is an additional benefit.

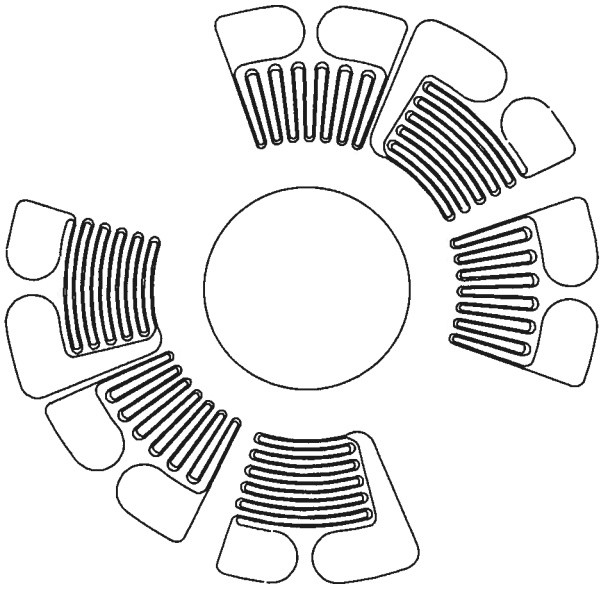

Figure 21 A layout of a 6-element combined radial and circumferential rosette.

Figure 22 shows strain sensitivity of the 6-element rosette, as indicated by the calibration coefficients $\bar{a}$ and $\bar{b}$ of the combined strain gauge is shown in . Calibration coefficient $\bar{a}$ increases by more than 130 % and calibration coefficient $\bar{b}$ increases by more than 60%. The increased strain sensitivity of the combined strain gauge is accomplished without any cost on the part of the stress calculation accuracy of the method for measuring non-uniform residual stress measurement. To examine the improvement of this new 6-element rosette relative to other three designs, especially to the rectangular one, the graphs of the reliability factors of these rosettes are shown in Figure 23. Figure 23 shows that the reliability factors for the 6-element rosette have greater values relative to corresponding values for the rectangular rosette. This means that measuring residual stresses by a 6-element rosette gives more accurate results in the same depth range which a rectangular rosettes gives reliable results. In addition, a 6-element rosette increases the practical depth limit for measuring residual stress variation with depth. For example, considering the values of F_{Ai} for rectangular rosette at depth equal to $0.7r_i$ as the criterion for acceptable accuracy, then as can be seen from Figure 23 the limit of measurement increases to depth equal to $0.9r_i$ which is 30% improvement.

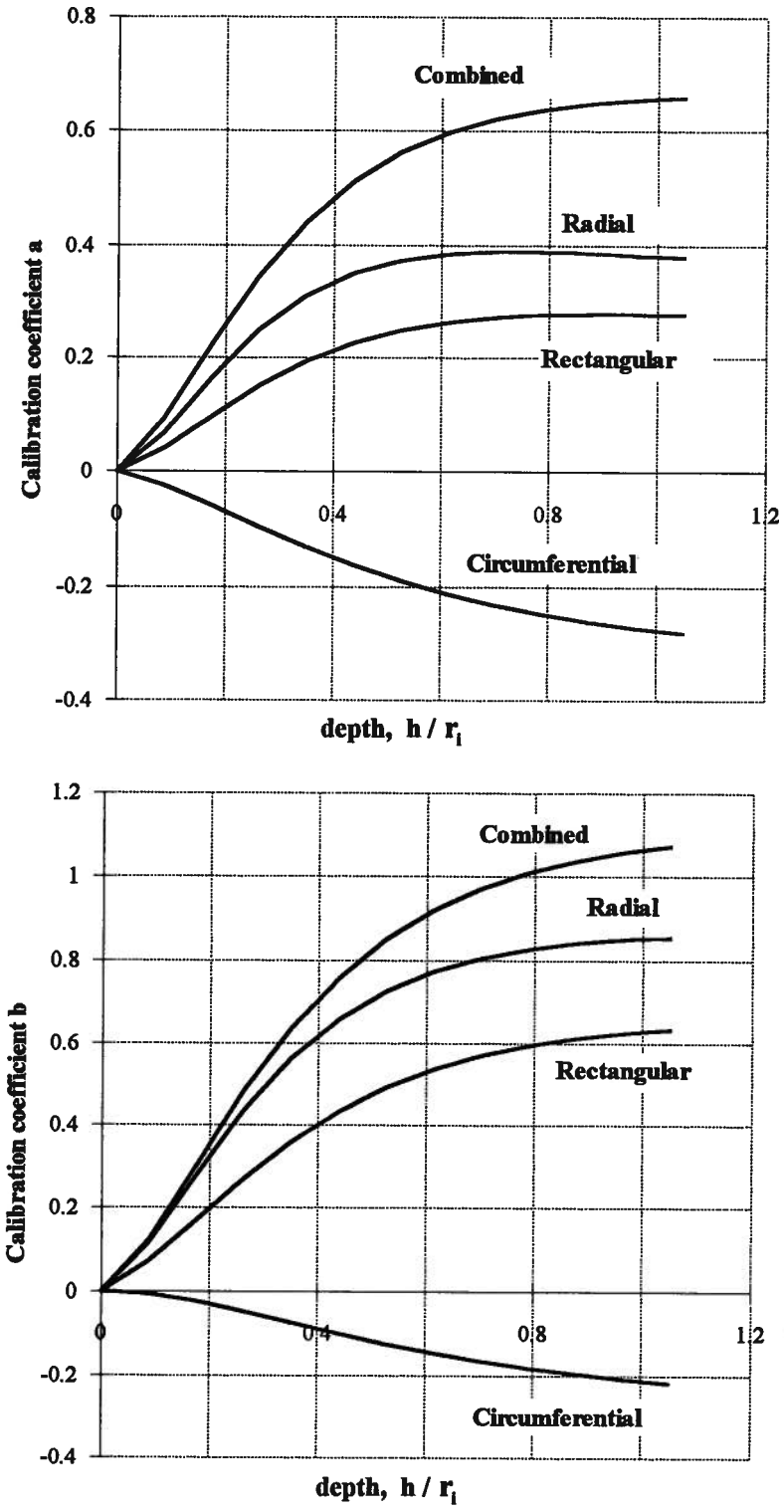

Figure 22 Calibration coefficient $\bar{a}$ and $\bar{b}$ for four different strain gauge designs.

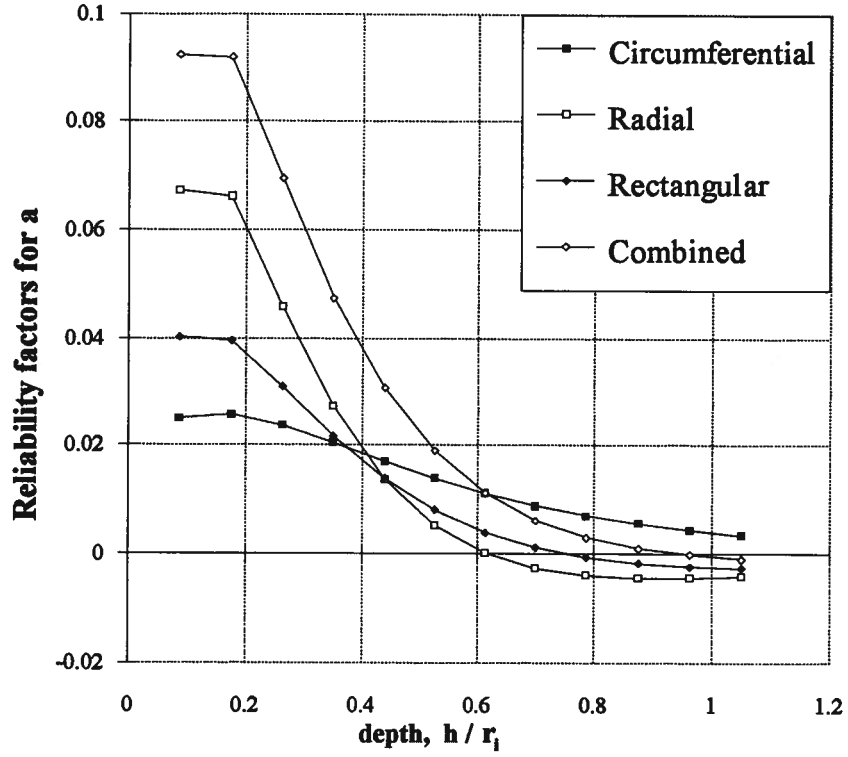

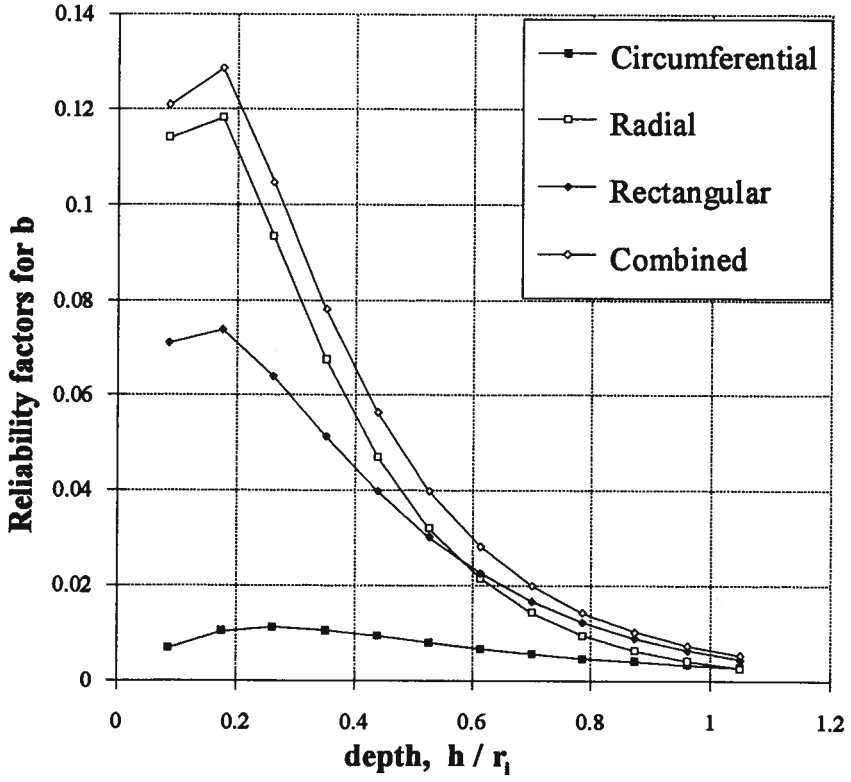

Figure 23 Reliability factors for four different strain gauge designs.

4.4 Experimental verification

To verify that the hole drilling method has a higher sensitivity using a 6-element rosette than a conventional ASTM rectangular rosette, a set of experiments similar to the experiments in Section 3.3 were conducted. One 6-element rosette and one rectangular RK-120 rosette were installed on a 12.7 x 38.1 x 565 mm aluminum bar. Similar precautions as mentioned in Section 3.3 were conducted to contain undesirable bending strains within 2%. The bar was subjected to a range of tensile loads from zero to 35 kN in 7 kN increments, and corresponding strains were recorded. The measured response of the strain gauges per unit load was determined from the gradient of the strain versus load plots. This procedure reduces the effect of random strain measurement errors and of any existing residual stresses.

Holes were drilled at the centers of the two strain gauge rosettes in 14 consecutive 0.20 mm depth increments. After drilling each increment, the sample was subjected to the same range of loads and the corresponding strains were recorded. Again, the response of the strain gauges per unit applied load was determined from the gradient of the strain versus load plots. After the drilling, the diameters of the hole at the centers of 6-element rosette and rectangular rosette were measured as 2.46 mm. From these data, the calibration coefficients $\bar{a}$ and $\bar{b}$ for a taper hole were evaluated using the method described by Rendler and Vigness [7].

Figure 24 compares the experimentally determined calibration coefficients $\bar{a}$ and $\bar{b}$ for the 6-element rosette with the corresponding ones for the standard RK-120 rosette. These graphs confirm that the 6-element rosette improved over the standard RK-120 rosette by more than 130% for calibration coefficient $\bar{a}$ and more than 60% for the calibration coefficients $\bar{b}$. In addition, the theoretical values $\bar{a}$ and $\bar{b}$ from finite element calculations for these two rosettes also are shown in Figure 24. The agreement between

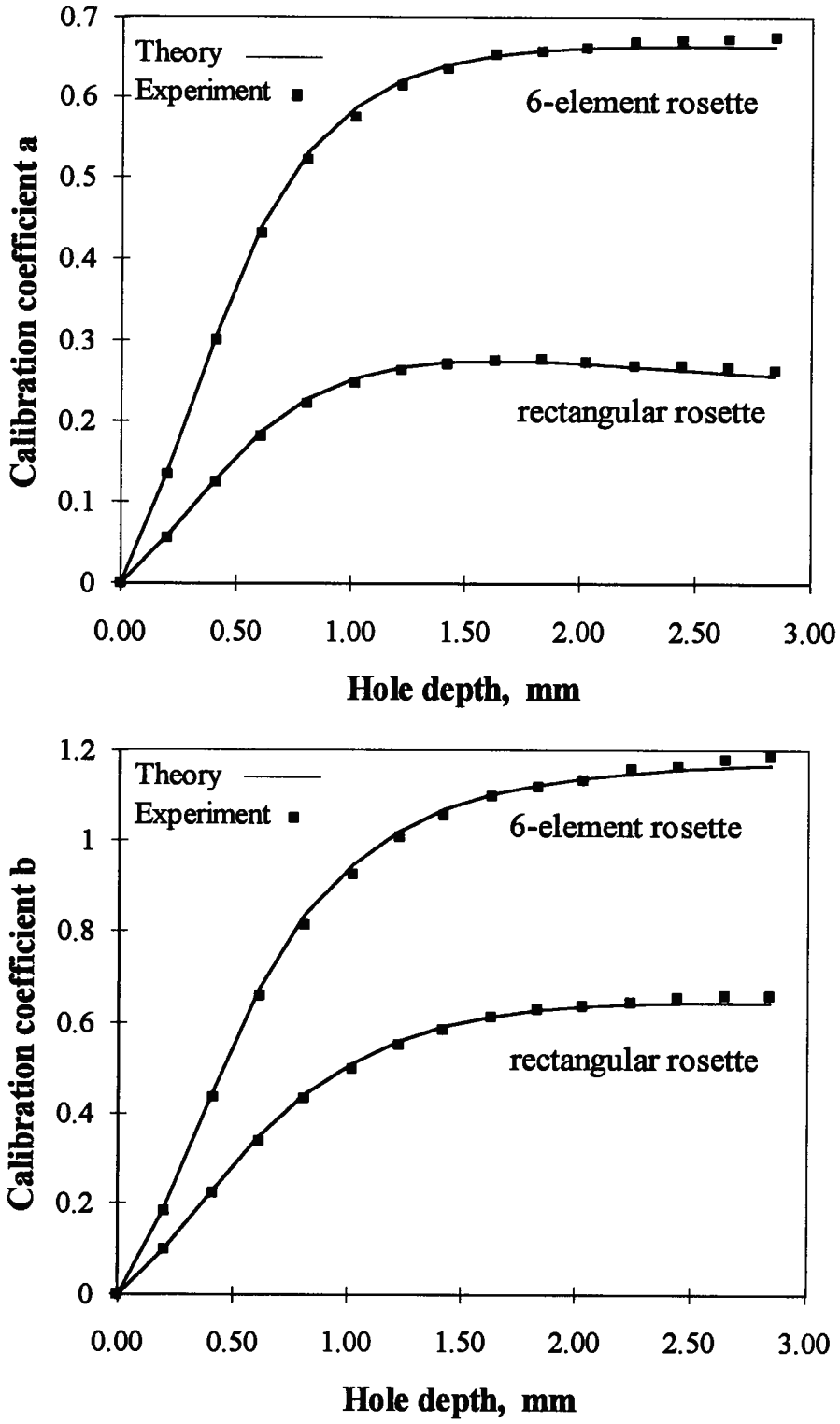

Figure 24 Comparison of experimental and theoretical $\bar{a}$ and $\bar{b}$ values for a 6-element rosette and a rectangular rosette.

numerically calculated calibration coefficients and their values determined by experiment were very good. The differences between experimental results and theoretical predictions are less than 3% for the 6-element rosette and 4% for RK-120 rosette. Note that in these graphs, the hole depth is specified in millimeters rather than normalized with respect to the mean rosette radius, r_m. This is done because the r_m values for the 6-element rosette and the standard rectangular rosette are different.

CHAPTER 5

CONCLUSION

The strain sensitivity and the accuracy of the hole-drilling method for measuring residual stresses was investigated in this study. This investigation focused on the effects of hole geometry and strain gauge rosette design. The study showed how these two features could be modified to improve the strain sensitivity and accuracy of the method.

This study demonstrated that the strain sensitivity can be improved significantly by modifying the geometry of the hole. Using of a reverse taper hole instead of straight hole was found to increase strain sensitivity by between 20-80%. This increased strain sensitivity reduces the effect of strain measurement errors on the residual stress calculation.

The sensitivity increase is mostly due to increased flexibility of the reverse taper hole compared with a straight hole of the same surface diameter. This flexibility contributes to faster stress relief in the area surrounding the hole. It also causes the strains around the hole to be relieved more rapidly which in turn make it possible to get the maximum possible strain reliefs and consequently maximum strain sensitivity in a relatively shallow hole compared with the straight hole case. Therefore, a higher sensitivity is achieved while less damage is done to the specimen. The practicality of taper hole drilling was demonstrated by designing and building a special taper hole drilling jig. The jig combined downward feed motion with and an off center orbiting.

Experiments were conducted to verify the theoretical results obtained from the finite element calculations. Agreement within 3% was achieved when comparing the finite element calculated calibration coefficients $\bar{a}$ and $\bar{b}$ for straight and taper holes with the corresponding experimentally determined values. This confirms that the finite element

procedure is effective in determining the calibration coefficients for the hole-drilling method. The experiments also verified that the specially designed taper hole drilling jig was able to drill reverse taper hole reliably. The jig was easy and convenient to use, and required only a small extra effort compared with straight hole drilling.

The second part of the thesis investigates the effects of the strain gauge rosette design on the strain sensitivity and accuracy of the hole drilling method. The strain sensitivity of radial and circumferential strain gauges was compared with that of conventional rectangular strain gauges. Calibration coefficients for these three different designs were evaluated. The relative merits of these designs for evaluating the variation of residual stresses with depth were investigated by studying their numerical conditioning and reliability factors.

A radial strain gauge rosette showed a significant improvement in strain sensitivity relative to the conventional rectangular design. Condition numbers of the radial strain gauge, however, were worse than the corresponding condition numbers for the rectangular strain gauge. The circumferential strain gauge, on the other hand, has relatively poor strain sensitivity, but has strong condition numbers. Because of its poor strain sensitivity the circumferential strain gauge is not suitable for measuring residual stresses when used alone.

A new 6-element rosette design is proposed which combines the beneficial characteristics of both radial and circumferential strain gauges. The new combined rosette has the benefit of higher strain sensitivity and temperature compensation. This 6-element design improves the calibration coefficients $\bar{a}$ by more than 130% and the calibration coefficients $\bar{b}$ by more than 60%. The 6-element rosette also improves the accuracy of the incremental method for measuring non-uniform residual stress fields and increases the maximum allowable depth by 30%.

A set of experiments was conducted to verify the higher strain sensitivity of the new 6-element design in practice. These experiments confirmed the theoretical results that the 6-element rosette has better strain sensitivity than the standard rectangular rosette, and that the theoretical method realistically models practical experimental measurements.

REFERENCES

(1) Mordfin, L. "Measurement of Residual Stresses: Problems and Opportunities," in Residual Stress for Designers and Metallurgists, Vande Walle, L. J. (editor), 1981, pp. 189-210

(2) Measurements Group, Inc. "Measurement of Residual Stresses by the Hole-Drilling Strain Gauge Method" Tech Note TN-503-4, Measurements Group, Inc., Raleigh, NC, 19pp., (1993).

(3) Mathar, J., "Determination of Initial Stresses by Measuring the Deformation around Drilled Holes," *trans., ASME 56*, No. 4, 1934, pp. 249-254

(4) Timoshenko, S. and Goodier, J. M. *Theory of Elasticity*, 3rd, ed., McGraw-Hill, New York, 1970.

(5) Soete, W. and Vancrombrugge, R. "An Industrial Method for the Determination of Residual Stresses," *Proceedings SESA*, Vol. 8, (1), 1950, 17-28.

(6) Kelsey, R. A. "Measuring Non-Uniform Residual Stresses by Hole Drilling Method," *Proceedings SESA*, Vol. 14, (1), 1956, pp. 181-194.

(7) Rendler, N. J. and Vigness, I. "Hole-drilling Strain-gage Method of Measuring Residual Stresses," Experimental Mechanics, Vol. 6, No. 12, December 1966, pp. 577-586

(8) American Society for Testing and Materials, "Standard Test Method for Determining Residual Stresses by the Hole-drilling Strain Gage Method," ASTM Standard E837-92 (1992).

(9) Beaney, E. M. and Procter, E. "A Critical Evaluation of the Center-Hole Technique for the Measurement of Residual Stresses," *Strain, Journal of BSSM,* Vol. 10, No. 1, 1974, pp. 7-14.

(10) Flaman, M. T., "Brief Investigation of Induced Drilling Stresses in the Center-Hole Method of Residual Stress Measurement," Experimental Mechanics, Vol. 22, No. 1, 1982, pp. 26-30.

(11) Schajer, G. S., "Application of Finite Element Calculation to Residual Stress Measurement." *Journal of Engineering Materials and Technology,* Vol. 103, April 1981, pp. 157-163

(12) Schajer, G. S., "Measurement of Non-Uniform Residual Stresses Using the Hole-Drilling Method. Parts 1 and 2," *Journal of Engineering Materials and Technology,* Vol. 110, October 1988, pp. 338-349

(13) Schajer, G. S., "Use of Displacement Data to Calculate Strain Gauge Response in Non-uniform Stress Fields," *Strain,* Vol. 29, No. 1, 1993. pp. 9-13

(14) Bijak-Zochowski, M. "A Semi-destructive Method of Measuring Residual Stresses," *VDI-Berichte,* Vol. 313, pp.469-476.

(15) Flaman, M. T. and Manning, B. H., "Determination of Residual Stress Variation with Depth by Hole-Drilling Method," *Experimental Mechanics,* Vol. 25, No. 9, 1985, pp. 205-207.

(16) Flaman, M. T., Mills, B. E., and Boag, J. M., "Analysis of Stress Variation with Depth Measurement Procedures for Center-Hole Method Residual Stress Measurement," *Experimental Techniques,* Vol. 11, No. 6, 1987, pp. 35-37.

APPENDIX

Calibration coefficients for a circumferential strain gauge

At each point of a single arc filament with the width w, radius r, and arc angle $\Delta\theta$ the circumferential strain is:

$$\varepsilon_\theta = \frac{u}{r} + \frac{dv}{rd\theta}$$

This strain changes the resistance dR in a infinitesimal arc $d\theta$ as:

$$\Delta\, dR = F\, \varepsilon_\theta\, dR = Fr\frac{rd\theta}{w}\varepsilon_\theta$$

Integrating over the arc length

$$\Delta R = \frac{F\rho r}{w}\int_{\theta_1}^{\theta_2}\left(\frac{u}{r} + \frac{dv}{rd\theta}\right)d\theta \qquad \text{(A1)}$$

For calibration coefficient A the displacement field is symmetrical, therefore for the ith filament:

$$\Delta R_i = \frac{F\Delta r_i}{w}\frac{u}{r}\int_{\theta_1}^{\theta_2} d\theta = \frac{F\rho u_i}{w}\Delta\theta$$

Total change of resistance for n filaments is:

$$\Delta R_T = \sum_{i=1}^{n}\Delta R_i = \frac{F\rho}{w}\Delta\theta\sum_{i=1}^{n}u_i$$

But $\Delta R_T = F R_T \varepsilon$, where R_T is the total original resistance of the grid and ε is average strain measured over the strain gauge. But $R_T = \frac{F\rho\Delta\theta}{w}\sum_{i=1}^{n} r_i$. Substituting in the above Equation gives:

$$\varepsilon = \frac{\sum u_i}{\sum r_i} \quad \Rightarrow \quad A = \frac{\sum u_i}{2\sum r_i} \tag{A2}$$

In the case of evaluating B: $u_i = U(r_i)\cos 2\theta$ and $v_i = V(r_i)\sin 2\theta$, then from Equation (A1):

$$\Delta R_i = \frac{F\rho r}{w}\int_{\theta_1}^{\theta_2}\left(\frac{u_i}{r_i} + \frac{dv_i}{r_i d\theta}\right)d\theta = \frac{F\rho r_i}{w}\int_{\theta_1}^{\theta_2}\left(\frac{U_i}{r_i}\cos 2\theta\, d\theta + \frac{1}{r_i}dv_i\right) =$$
$$2\frac{F\rho r_i}{w}\frac{u_i + 2v_i}{2r_i}\sin\Delta\theta\cos 2\varphi = \frac{F\rho}{w}(u_i + 2v_i)\sin\Delta\theta\cos 2\varphi$$

where φ is angle between the mid radial axis and the principal stress direction. Then B can be calculated as follow:

$$\Delta R_T = \sum_{i=1}^{n}\Delta R_i = \frac{F\rho}{w}\sin\Delta\theta\cos 2\varphi\sum_{i=1}^{n}(U_i + 2V_i) = FR_T\varepsilon$$
$$= \frac{F\rho}{w}\varepsilon\sum r_i\Delta\theta$$

$$\Rightarrow \quad \varepsilon = \frac{\sum(U_i + 2V_i)\sin\Delta\theta\cos 2\varphi}{\sum r_i\Delta\theta}$$

$$\Rightarrow \quad B = \frac{\varepsilon}{2\cos 2\varphi} = \frac{\sum(U_i + 2V_i)}{\sum r_i}\frac{\sin\Delta\theta}{\Delta\theta} \tag{A3}$$